

CHIMERA: Adaptive Cache Injection and Semantic Anchor Prompting for Zero-shot Image Morphing with Morphing-oriented Metrics

Dahyeon Kye^{*,1} Jeahun Sung^{*,1} Minkyu Jeon² Jihyong Oh^{†,1}

¹ CMLab, Chung-Ang University ² Princeton University

{rpekgus, jhseong, jihyongoh}@cau.ac.kr mj7341@princeton.edu

<https://cmlab-korea.github.io/CHIMERA/>

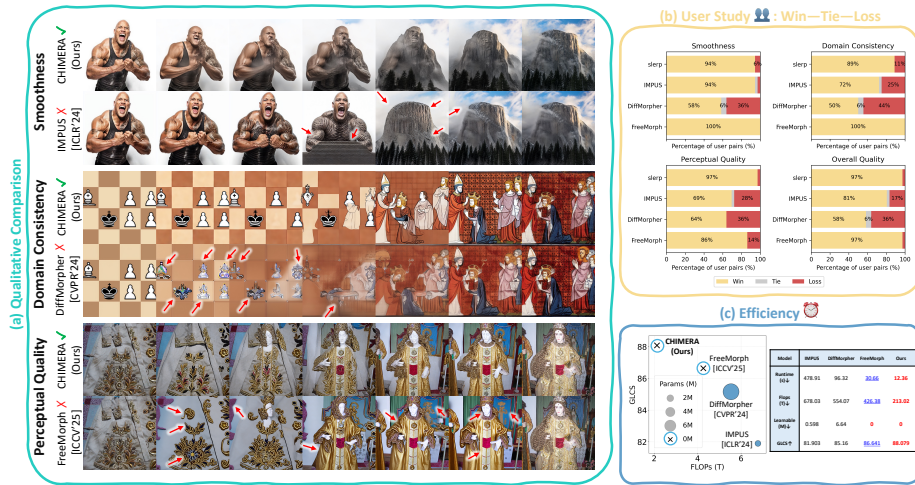


Fig. 1: Given two input images, **CHIMERA** generates perceptually smooth transitions while jointly satisfying three key criteria: *Smoothness*, *Domain Consistency*, and *Perceptual Quality* (left; red arrows highlight failure modes of prior methods). Our user study further shows that CHIMERA is consistently preferred over baselines across all criteria, and this preference trend aligns with *our morphing-oriented metric, GLCS*. Finally, CHIMERA is training-free and efficient, achieving favorable runtime and computational cost compared to tuning-based approaches (right).

* Equal contribution.

† Corresponding author.

Abstract. Recent diffusion-based image morphing methods typically interpolate inverted latents and reuse limited conditioning signals, which often yields unstable intermediates for heterogeneous endpoint pairs. In particular, (i) feature reuse is usually partial or non-adaptive, leading to abrupt structural changes or over-smoothing, and (ii) text conditions are commonly obtained independently per endpoint and then interpolated, which can introduce incompatible semantics. We present CHIMERA, a novel zero-shot diffusion morphing framework that addresses both issues via inversion-guided denoising with complementary feature reuse and text conditioning. ACI caches a broader set of multi-scale diffusion features beyond Key-Value-only reuse during DDIM inversion, and re-injects them with layer- and timestep-aware scheduling to stabilize denoising and enable gradual fusion. Semantic Anchor Prompting (SAP) uses a vision-language model to generate a shared anchor-prompt and anchor-conditioned endpoint prompts, and injects the anchor into cross-attention to improve intermediate semantic coherence. Finally, we propose Global-Local Consistency Score (GLCS), a morphing-oriented metric that jointly captures global domain harmonization and local transition smoothness. Extensive experiments and user study show that CHIMERA produces smoother and more semantically consistent morphs than prior methods, while remaining efficient and applicable across diverse diffusion backbones without retraining. Code and the project page will be released.

Keywords: Image morphing · Image generation · Diffusion model

1 Introduction

Image morphing generates perceptually and semantically smooth transitions between two images. It is widely used in animation, film, and design, where intermediates must remain visually plausible and semantically meaningful [1, 67]. Classical pipelines typically rely on handcrafted correspondences or optical-flow-based warping [56], which often fail for input pairs with large structural or domain gaps. Recent extensions to 3D morphing [33, 51] further highlight the growing importance of robust morphing across modalities.

Recent diffusion-based morphing [5, 53, 55, 59, 62] improves fidelity via latent-space interpolation of pre-trained diffusion models [43, 48] without explicit correspondence estimation. However, they remain unstable for heterogeneous or cross-domain inputs (e.g., photographs vs. illustrations) [13, 19], often exhibiting structural inconsistency, semantic drift, or over-saturated artifacts. We argue that a successful morphing should satisfy three criteria simultaneously: (i) **Smoothness**, (ii) **Domain Consistency**, and (iii) **Perceptual Quality**. As shown in Fig. 1, prior methods typically satisfy only a subset.

A key limitation of prior methods is insufficient transfer of input pair information to the denoising process. Tuning-based methods (e.g., IMPUS [59]) improve semantics but incur substantial per-pair optimization cost, while diffusion feature reuse methods (e.g., DiffMorpher [62] and FreeMorph [5]) primarily

rely on Key/Value features from self-attention layers. We show that this KV-only reuse is a key contributing factor in their failure to satisfy both smoothness and domain consistency simultaneously. To support this, we analyze the similarity between diffusion features of the input pair and those of generated morphing images (Sec. 3), and observe that reusing only specific features is insufficient for stable and coherent morphing.

To preserve the efficiency of training-free morphing while overcoming these limitations, we propose **CHIMERA** (**CacHe Injection and SeMantic Anchor Prompting for ZERo-shot ImAge Morphing with Morphing-oriented Metrics**), a novel zero-shot diffusion-based image morphing framework. CHIMERA is built on two complementary components: **Adaptive Cache Injection (ACI)** and **Semantic Anchor Prompting (SAP)**.

ACI improves feature reuse by leveraging multi-scale diffusion features beyond the KV-only used in prior methods [5, 62]. Rather than naively injecting all cached features, ACI performs frequency-aware layer-timestep alignment via **Layer- and Timestep-wise Frequency Matching (LTM)**, enabling appropriate feature reuse at appropriate denoising steps. This design stabilizes structure and appearance transitions, improving domain consistency and smoothness while preserving fidelity.

Morphing remains difficult when the input pair shares little semantic or structural overlap. To address this, SAP uses a VLM [2, 32] to identify the shared semantic/structural intersection (i.e., an *anchor*) of the input pair and to construct anchor-correlated prompts. In contrast to prior methods that generate endpoint prompts independently, SAP constructs morphing-aware prompts, improving semantic coherence and reducing ambiguity in text conditioning.

Finally, we extend our analysis method (Fig. 2) to define a morphing-oriented metric, **Global-Local Consistency Score (GLCS)**, which jointly quantifies global domain harmonization and local transition smoothness. Unlike conventional metrics that capture only partial aspects of morphing quality, GLCS offers a unified measure that better reflects perceptual morphing quality. Our main contributions are summarized as follows:

- We propose **CHIMERA**, a novel zero-shot diffusion morphing framework combining adaptive inversion-cache reuse and semantic anchor prompting for smooth and semantically coherent transitions.
- We propose **Adaptive Cache Injection (ACI)**, a layer- and timestep-adaptive diffusion feature reuse strategy that enables stable sampling and gradual, coherent fusion of structure and appearance.
- We propose **Semantic Anchor Prompting (SAP)**, which derives anchor-correlated prompts from a VLM to improve intermediate coherence and reduce semantic drift.
- We show that CHIMERA is training-free, efficient, and backbone-agnostic across diffusion models, while remaining competitive with tuning-based morphing methods.
- We propose **Global-Local Consistency Score (GLCS)**, a morphing-oriented metric that jointly measures global domain harmonization and local

transition smoothness, and better aligns with human preference than conventional metrics in our user study.

2 Related Work

2.1 Image Morphing

Image morphing is a long-standing problem in computer vision and graphics [1, 56], aiming for perceptually smooth transitions between two images. Early approaches based on geometric correspondences (e.g., feature-line interpolation or flow-based warping) often break when the input pair exhibits large appearance or semantic gaps, yielding ghosting or distorted intermediates [3, 25]. Tuning-based methods improve morphing quality but can suffer from limited generalization due to task- or class-specific training data [30, 42]. Recent diffusion-based methods exploit generative priors for latent-space morphing [5, 59, 62], yet remain unreliable on highly heterogeneous pairs, partly due to limited adaptability and architecture-specific reuse designs. To address this, we propose a backbone-agnostic framework that stabilizes denoising via timestep- and layer-wise adaptive inversion-cache reuse and improves semantic coherence with an anchor-correlated prompt triplet.

2.2 Diffusion Latents and Feature Reuse

Diffusion models [12, 17, 49] produce hierarchical U-Net features during denoising [44]. These intermediate representations encode geometric and semantic cues [21, 40] and are widely used for generation control and stabilization via feature-level guidance/modulation [10, 15, 18, 26, 52, 63]. More specifically, previous morphing methods such as DiffMorpher [62] and FreeMorph [5] reuse attention-layer Key and Value features to preserve structure, texture, or source identity. In contrast, we argue that broader diffusion feature reuse across layers yields more stable morphing in terms of domain consistency and smoothness (Sec. 3), which motivates ACI.

2.3 Text-guided Diffusion Models

Text-conditioned diffusion models provide a strong prior for controllable generation, where text token embeddings modulate features via cross-attention. VLMs [2, 32, 41] align visual and textual semantics, enabling captioning and semantic control widely used in text-guided editing and attention-based manipulation [5, 7, 36, 62]. In diffusion-based morphing, endpoint prompts are often obtained independently and then interpolated during sampling [5, 59, 62]. For heterogeneous pairs, such independently formed prompts can yield conflicting conditioning cues and causing semantic drift in intermediate states. To overcome this, we use a VLM to extract a shared anchor and produce anchor-conditioned endpoint prompts, forming an anchor-correlated prompt triplet.

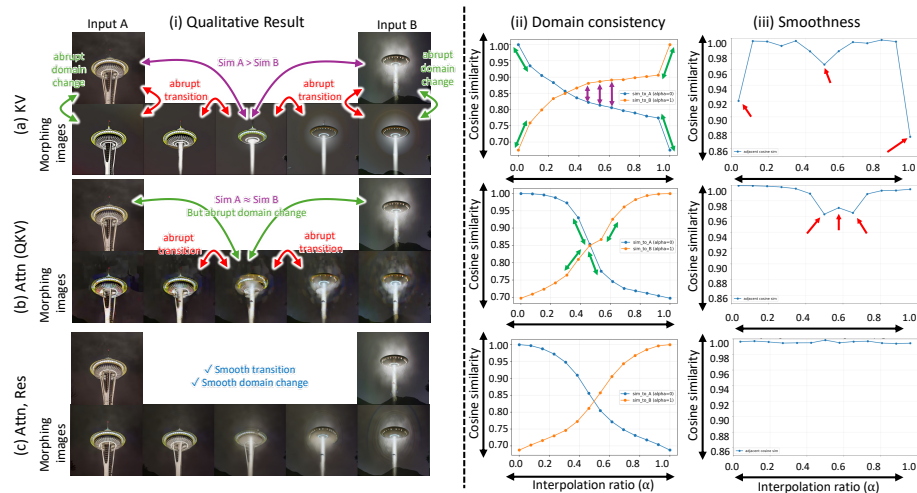


Fig. 2: Observation on diffusion feature reuse. (a) reuses only attention-layer Key/Value features (KV), (b) reuses attention features including Query (Attn; QKV), and (c) further includes ResNet features (Attn, Res). (i) shows qualitative results, (ii) reports domain consistency, and (iii) reports smoothness. The results in (ii) and (iii) are averaged over the Morph4Data [5] dataset.

3 Observations

Why We Reuse a Broader Set of Diffusion Features. Before introducing Adaptive Cache Injection (ACI), we analyze whether reusing only partial diffusion features (such as the attention-layer KV features used in DiffMorpher [62] and FreeMorph [5]) is sufficient, or whether broader diffusion feature reuse is more desirable. Fig. 2 compares three settings: (a) KV-only reuse, (b) reuse of the full attention features (including Query), and (c) extended diffusion feature reuse including additional ResNet features. We analyze domain consistency and smoothness at the feature level using DiffSim [50]. Specifically, Fig. 2-(ii) measures the similarity between each morphing feature and the endpoint features (A , B) to evaluate domain consistency, while Fig. 2-(iii) measures the similarity between adjacent morphing features to evaluate smoothness. Ideally, the similarity curves to the two endpoints intersect near $\alpha = 0.5$ and vary smoothly along the interpolation trajectory, while the similarity between adjacent frames changes gradually without large oscillations. As shown in Fig. 2-(a), KV-only reuse leads to overly strong endpoint transitions (green arrow), a bias of the middle frame toward one domain (purple arrow), and significant drops in smoothness at certain points (red arrow). Including the entire attention feature in Fig. 2-(b) alleviates these issues, and further incorporating ResNet features in Fig. 2-(c) stabilizes both curves. These trends are also reflected in the qualitative results in Fig. 2-(i). Overall, these observations suggest that broader diffusion feature reuse provides more stable morphing guidance than KV-only reuse, motivating the design of ACI. Furthermore, this analysis method provides a unified perspective for un-

derstanding domain consistency and smoothness. Based on this observation, we extend it to define a single quantitative metric, GLCS (Sec. 4.3).

How We Reuse Diffusion Features. Broader diffusion feature reuse is beneficial, but injecting all layers naively is unstable. To address this limitation, we analyze DDIM inversion features and denoising timesteps in Stable Diffusion 2.1 [43] from a frequency-domain perspective (Fourier domain).

As shown in Fig. 3, mid-block inversion features are dominated by low-frequency components, whereas up-block features contain stronger high-frequency components; likewise, early timesteps emphasize low-frequency structures while later timesteps focus on high-frequency details. Accordingly, we inject mid-block features at early timesteps and up-block features at later timesteps. We implement this as Layer- and Timestep-wise Frequency Matching (LTM) in ACI, which jointly considers layer-wise feature spectra and timestep-wise denoising properties. While Fig. 3 reports SD2.1, we find the same coarse-to-fine frequency shift across timesteps to be consistent across backbones (see Sec. 5.3 and *Suppl.*).

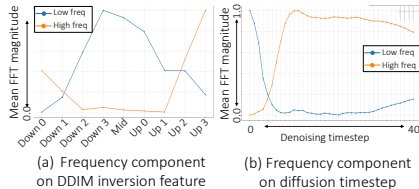


Fig. 3: Frequency analysis of diffusion features and denoising timesteps. Low- (blue) and high-frequency (orange) components across (a) U-Net feature layers and (b) DDIM denoising timesteps are measured for the base model without CHIMERA’s ACI and SAP on Morph4Data [5]. Values are obtained by applying FFT with masked frequency bands.

4 Proposed Method: CHIMERA

Overall Pipeline. As shown in Fig. 4, given input images A and B , DDIM inversion (DDIM) [48] projects them into the latent space to obtain $z_A = \text{DDIM}(A)$ and $z_B = \text{DDIM}(B)$. Spherical interpolation (`slerp`) [47] then yields the K -morphing latents $z_k = \text{slerp}(z_A, z_B; \alpha_k)$, $k = 0, \dots, K - 1$, where α_k denotes the interpolation weight, K is the number of intermediate morphing latents, and k denotes the index of `slerp`.

During DDIM of A and B , we cache multi-scale U-Net features. Specifically, we record the down, mid, and up features as:

$$H_S(X, t), \quad S \in \{\mathbf{D}, \mathbf{M}, \mathbf{U}\}, X \in \{A, B\}, t \in T_{\text{inv}}, \quad (1)$$

where H_S denotes the multi-scale U-Net features and \mathbf{D} , \mathbf{M} , \mathbf{U} represent down-sampling, mid, and upsampling blocks. Here, $T_{\text{inv}} = (t_0^{\text{inv}}, \dots, t_{N_{\text{inv}}-1}^{\text{inv}})$ denotes the set of inversion timesteps, where N_{inv} is the number of inversion timesteps. To align the characteristics of layers with those of timesteps, we introduce Layer- and Timestep-wise Frequency Matching (LTM). The aligned cached multi-scale

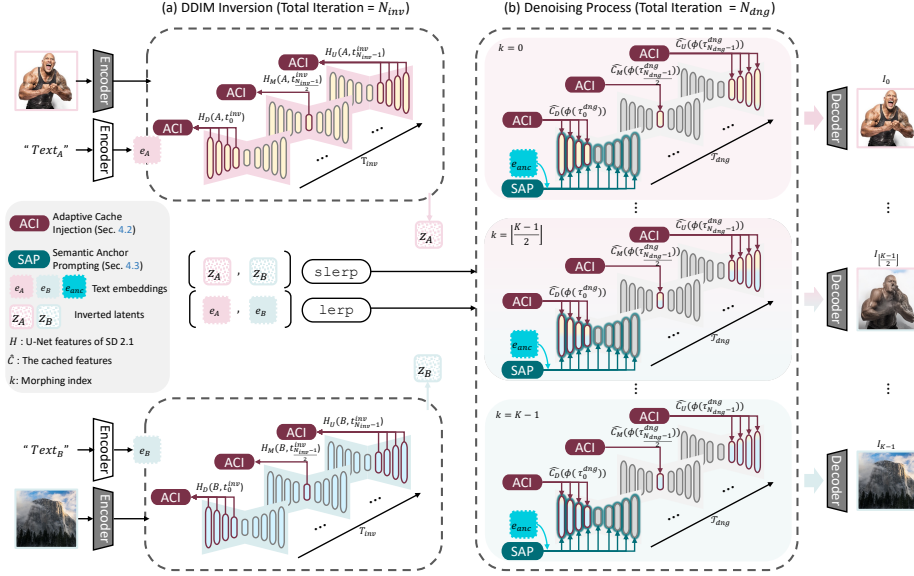


Fig. 4: Overview of CHIMERA. (a) DDIM Inversion: Inputs A and B are inverted while caching multi-scale U-Net features from the down, mid, and up blocks. The cached features are interpolated via `slerp`, forming morphing-aligned latents. (b) Denoising: The interpolated caches are re-injected through ACI. ACI adaptively injects cached features by applying LTM based on the observations in Fig. 3. In addition, SAP introduces a VLM-derived anchor-prompt into early cross-attention layers, stabilizing semantics. The full algorithm is provided in Algorithm 1 of the *Suppl.*

feature is denoted as $H_{S^*}(X, t)$. We then apply `slerp` to the cached features:

$$\widehat{C}_{S^*}(k, t) = \text{slerp}(H_{S^*}(A, t), H_{S^*}(B, t); \alpha_k), \quad (2)$$

where $\widehat{C}_{S^*}(k, t)$ denotes interpolated cached U-Net feature, k denotes the `slerp` index and t denotes the DDIM timestep. These features are then injected into the U-Net during the denoising process according to their matched timesteps.

4.1 Adaptive Cache Injection (ACI)

As discussed in Sec. 3, reusing only the Key and Value features from attention layers cannot guarantee both domain consistency and smoothness. To overcome this limitation, we propose Adaptive Cache Injection (ACI), which adaptively leverages all diffusion layers.

As described in Sec. 4, during DDIM, we cache down (**D**), mid (**M**), and up (**U**) features for each input (see Eq. 1), and blend the cached features from A and B via Eq. 2 for each morphing index k . However, naively reusing all cached layers at all timesteps does not guarantee stable performance. To address this issue, we introduce **Layer- and Timestep-wise Frequency Matching (LTM)**, which

constructs a frequency-based layer–timestep correspondence *during the caching stage* based on the observations in Sec. 3.

Specifically, for a feature tensor $Z \in \mathbb{R}^{C \times H \times W}$, we quantify its spectral property using an FFT-magnitude descriptor $\mathbf{r}(Z) = \text{Pool}\left(\frac{1}{C} \sum_{c=1}^C |\mathcal{F}(Z_c)|\right)$, where $\mathcal{F}(\cdot)$ denotes 2D FFT and $\text{Pool}(\cdot)$ is radial (band-wise) pooling. Using cached inversion features $H_S(X, t)$, we construct frequency prototypes for each layer group $S \in \{\mathbf{D}, \mathbf{M}, \mathbf{U}\}$ and each inversion timestep $t \in \mathcal{T}_{\text{inv}}$, denoted by $\bar{\mathbf{r}}_S$ and $\bar{\mathbf{r}}_t$, respectively. We then measure their frequency discrepancy by $D_{S,t} = d(\bar{\mathbf{r}}_S, \bar{\mathbf{r}}_t)$, where $d(\cdot, \cdot)$ is an ℓ_1 distance. Based on $D_{S,t}$, LTM builds a layer-timestep correspondence by matching each timestep to the most frequency-consistent layer group $S^*(t) = \arg \min_{S \in \{\mathbf{D}, \mathbf{M}, \mathbf{U}\}} D_{S,t}$. This precomputed correspondence is used to organize and select cache entries for later ACI injection, enabling frequency-aware feature reuse that better preserves domain consistency and transition smoothness. We then sequentially inject the cached features obtained above into the denoising process. However, in our experimental setting, the number of timesteps in DDIM inversion differs from that of the denoising process. To align the cached features from specific DDIM inversion timesteps with the denoising timesteps, we introduce Inversion-Denoising Timestep Mapping (IDM), which linearly maps each denoising step τ to an inversion timestep $t = \phi(\tau)$. We denote the mapped cached features of images A and B as $H_{S^*}(A, \phi(\tau))$ and $H_{S^*}(B, \phi(\tau))$, respectively. By applying `slerp` to these two features, the final cached feature injected into the denoising process is expressed as follows:

$$\hat{C}_{S^*}(k, \tau) = \text{slerp}(H_{S^*}(A, \phi(\tau)), H_{S^*}(B, \phi(\tau)); \alpha_k). \quad (3)$$

The cached feature \hat{C}_{S^*} is multiplied by the blending weight λ_S and then added as a residual $\tilde{F}_S^{(\tau)} = F_S^{(\tau)} + \lambda_S \cdot \hat{C}_{S^*}(\phi(\tau))$, where F_S denotes the denoising feature at layer S , and \tilde{F}_S represents the feature after adding the cached feature as a residual. Through this overall process, ACI provides *layer-wise* and *timestep-aware* aligned guidance, enabling the generation of smooth and coherent morphing.

4.2 Semantic Anchor-Prompting (SAP)

ACI stabilizes morphing by feature reuse, but semantic coherence can still degrade when the inputs are *heterogeneous*. In particular, diffusion-based morphing often relies on independently obtained endpoint prompts and interpolates them during sampling, which may yield incompatible or unbalanced textual conditions for intermediates. To address this, we propose Semantic Anchor-Prompting (SAP), which constructs an anchor-correlated prompt triplet for the input pair and injects the semantically shared anchor-prompt as an auxiliary conditioning in cross-attention to provide a stable semantic guidance.

Table 1: Average cosine similarity between anchor and endpoint prompts (Morph4Data).

Text Prompt	Shared Anchor-prompt	Unshared Anchor-prompt
$text_A$	0.561	0.405
$text_B$	0.557	0.398

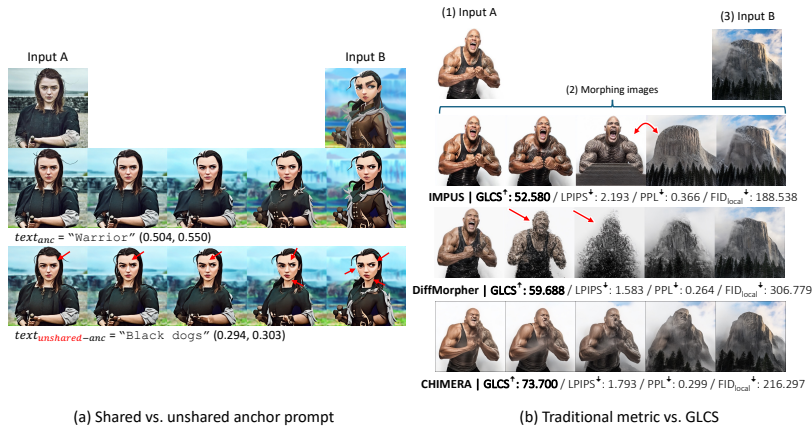


Fig. 5: (a): Effect of shared vs. unshared anchor-prompts. The second row uses a shared anchor-prompt, while the third row uses an intentionally unshared anchor-prompt. The two numbers in parentheses denote *cossim* between the anchor-prompt and each endpoint prompt, respectively. Red arrows highlight artifacts under unshared anchors. **(b): Traditional metric vs. GLCS.** Given input image pairs (1) and (3), different methods produce morphing sequences shown in (2), highlighting cases where GLCS successfully reflects differences in global–local consistency that are not fully captured by conventional metrics.

Anchor-correlated Prompt Triplet. Given an input pair, we query a VLM [2] with a structured instruction to generate an anchor-correlated prompt triplet $(text_{anc}, text_A, text_B)$. The anchor-prompt $text_{anc}$ captures the shared semantic or structural concept of the pair, while the endpoint prompts $text_A$ and $text_B$ describe each input while preserving the anchor. Unlike prior pipelines that obtain endpoint prompts independently [5, 59, 62], this anchor-conditioned prompt construction explicitly encourages semantic overlap between the endpoint prompts, making the subsequent interpolation and text conditioning more reliable. We encode $(text_{anc}, text_A, text_B)$ using the CLIP text encoder [41] to obtain embeddings $(\mathbf{e}_{anc}, \mathbf{e}_A, \mathbf{e}_B)$, and denote the cosine similarity as *cossim*. Following prior findings on the local linearity of CLIP’s embedding space [4, 27, 36, 59], semantically related prompts tend to yield closer embeddings, which supports more stable endpoint prompt interpolation. Consistent with this, Fig. 5 (a) shows that an unshared anchor-prompt (low *cossim* to the endpoints) leads to degraded morphing quality, e.g., facial distortions. Table 1 further confirms that shared anchors exhibit higher similarity to both endpoints than unshared anchors. Accordingly, we re-query the VLM until the anchor satisfies an anchor-reliability criterion (e.g., $cossim \geq 0.45$); the full VLM instruction, prompt examples, and the complete procedure are provided in the *Suppl.*

Anchor-guided Cross-Attention. SAP injects the anchor-prompt as auxiliary conditioning into the cross-attention, where text tokens directly modulate spatial features. At a denoising step τ , the endpoint and anchor embeddings are

projected to (K_A, V_A) , (K_B, V_B) , and $(K_{\text{anc}}, V_{\text{anc}})$, and the anchor Key-Value is concatenated to each endpoint branch:

$$\text{Attn}_X = \text{softmax}\left(\frac{Q[K_X \| K_{\text{anc}}]^\top}{\sqrt{d}}\right) [V_X \| V_{\text{anc}}], \quad X \in \{A, B\}, \quad (4)$$

where Q is the Query from the current diffusion feature and d is the attention dimension. This anchor-guided design encourages intermediate features to remain compatible with the semantics shared by both endpoints, reducing drift toward either side. We activate SAP only at early denoising timesteps to avoid over-constraining fine details, as validated by the ablation in the *Suppl.*

4.3 Global-Local Consistency Score (GLCS)

Motivation. $\text{FID}_{\text{local}}$ [16], $\text{FID}_{\text{global}}$ [16], LPIPS [64], and PPL [20] are widely used for quantitative morphing evaluation (see Fig. 5). However, they often misalign with perceived morphing quality. LPIPS and PPL only measure adjacent-image similarity, and thus sequences that deviate from the input images A and B can still score well if local changes are small. For example, in Fig. 5-(b)-(2), the *second* row yields lower LPIPS and PPL than the *third*, even though the latter is visually superior. $\text{FID}_{\text{local}}$ also fails to reflect perceptual domain consistency, as it averages the distribution gap between A, B and all intermediates without considering the interpolation ratio. Consequently, it often favors images that resemble both inputs simultaneously rather than those forming a natural transition. As shown in Fig. 5-(b)-(2), $\text{FID}_{\text{local}}$ incorrectly prefers the *first* row over the *third*, even though the third better preserves the domain characteristics (e.g., stone texture and facial identity). To address these issues, we propose the Global-Local Consistency Score (GLCS), motivated by the observations in Sec. 3, where the domain-consistency and smoothness analysis align well with human perception. GLCS further shows 80% agreement with user study preferences (Sec. 5.1), providing a morphing-specific metric that jointly measures domain consistency and smoothness.

Proposed Metric. We propose Global-Local Consistency Score to evaluate morphing quality with two complementary factors. First, the Global Consistency Score (GCS) measures domain consistency. It checks whether each image follows the expected global trend between the two input images A and B . We obtain this trend by interpolating the endpoint similarities with `slerp`, so the sequence should change in a balanced way from A to B . Second, the Local Consistency Score (LCS) measures *smoothness*. It checks whether the similarity of each image changes smoothly with respect to its neighbors. Thus, LCS captures local continuity along the morphing transition. We use a DiffSim-based [50] bounded similarity $s(\cdot, \cdot)$, which is sensitive to low-level structure and also reflects style and semantic similarity. Both GCS and LCS are clamped to $[0, 1]$ for stability and interpretability. GLCS combines these two perspectives and is high only when the sequence is globally well-mixed and locally smooth $\text{GLCS} = \sqrt{\text{GCS} \cdot \text{LCS}}$. For detailed explanations of GLCS, the algorithm, edge-case analyses of LCS and GCS, and additional qualitative results, please refer to the *Suppl.*

Table 2: Quantitative results on Morph4Data and MorphBench datasets. The best scores are marked in bold, while the second best are underlined.

Morph4Data						MorphBench					
Model name	FID _{local} ↓	FID _{global} ↓	LPIPS ↓	PPL ↓	GLCS ↑	Model name	FID _{local} ↓	FID _{global} ↓	LPIPS ↓	PPL ↓	GLCS ↑
IMPUS	150.1332	70.231	1.9125	0.3188	81.9027	IMPUS	93.417	44.287	1.296	0.216	89.426
DiffMorpher	181.9924	92.5483	<u>1.6378</u>	<u>0.273</u>	85.1597	DiffMorpher	133.086	62.1269	<u>1.044</u>	<u>0.174</u>	<u>91.887</u>
FreeMorph	191.3487	98.4444	1.9731	0.3289	<u>86.6412</u>	FreeMorph	148.972	81.019	1.494	0.249	90.566
CHIMERA	<u>161.054</u>	<u>82.308</u>	1.576	0.263	88.079	CHIMERA	<u>117.173</u>	<u>58.619</u>	1.029	0.161	93.180

5 Experiment

Implementation Details. Our proposed model, CHIMERA, is based on Stable Diffusion 2.1 [43]. For ACI, we use $N_{inv} = 50$ DDIM inversion timesteps and $N_{dng} = 50$ denoising timesteps. The cached features are weighted with $\lambda_S = 0.4$. For SAP, we use Qwen2.5-VL [2] as the VLM. Further implementation details are provided in the *Suppl.* for reproducibility.

Evaluation Datasets. MorphBench [62] contains 90 object pairs covering object metamorphosis and animation-style continuous transformations. Morph4Data [5] expands diversity with broader semantic and layout variations, including similar-layout/different-semantic pairs, aligned-semantic pairs (e.g., faces, cars), random ImageNet-1K [45] pairs, and dog–cat pairs collected online.

Evaluation Metrics. We conduct quantitative evaluation using the metrics adopted in prior methods [5, 59, 62], including FID_{local} [16], FID_{global} [16], LPIPS [64], PPL [20], and our proposed GLCS. For detailed definitions and evaluation protocols, please refer to the *Suppl.*

5.1 Quantitative and Qualitative Evaluations

Quantitative Evaluation. We evaluate CHIMERA using the standard metrics adopted in prior morphing methods [5, 59, 62], including FID_{global}, FID_{local}, LPIPS, and PPL, together with our proposed GLCS. Table 2 reports results for 7-frame morphing. As shown in the table, existing methods exhibit a clear trade-off. IMPUS achieves strong performance on FID_{local} and FID_{global}, but records low LPIPS, PPL, and GLCS scores, indicating abrupt transitions. DiffMorpher achieves the best LPIPS and PPL, yet its FID and GLCS scores are lower, suggesting weak domain consistency. FreeMorph performs poorly on conventional metrics due to over-smoothing and excessive color saturation. However, because transitions between adjacent images are relatively smooth, it attains comparatively competitive GLCS results. In contrast, CHIMERA achieves balanced performance across FID_{local}, FID_{global}, LPIPS, and PPL. It significantly outperforms the zero-shot baseline FreeMorph and achieves results competitive with tuning-based methods. Moreover, CHIMERA attains the highest GLCS, LPIPS and PPL scores on both Morph4Data and MorphBench, demonstrating strong domain consistency and smoothness simultaneously. Additional quantitative results for the 16-frame setting are provided in the *Suppl.*

User Study. In a user study under four perceptual criteria, CHIMERA is consistently preferred over all baselines. Fig. 1 (b) shows the pairwise win–tie–loss

Table 3: Ablation study on caching block and layer types. Left: ablation over the major diffusion blocks, namely the down, mid, and up blocks. Right: ablation study on the layers within each diffusion block. The layers are categorized into Key and Value features, Attention layers, and ResNet features.

ACI Ablation - Block type						ACI ablation - Layer type					
Block	FID _{local} ↓	FID _{global} ↓	LPIPS ↓	PPL ↓	GLCS ↑	Layer	FID _{local} ↓	FID _{global} ↓	LPIPS ↓	PPL ↓	GLCS ↑
(a) {D}	181.560	92.174	1.8021	0.3003	87.904	(a) KV	209.809	102.093	1.908	0.318	87.096
(b) {D, M}	<u>178.256</u>	<u>89.889</u>	<u>1.740</u>	<u>0.292</u>	<u>87.886</u>	(b) Attn	<u>183.486</u>	<u>92.829</u>	<u>1.785</u>	<u>0.298</u>	<u>87.159</u>
(c) {D, M, U} (Ours)	161.054	82.308	1.576	0.263	88.079	(d) Attn, Res (Ours)	161.054	82.308	1.576	0.263	88.079

outcomes, where CHIMERA wins against FreeMorph and latent `slerp` in most cases and records more wins than losses against DiffMorpher and IMPUS. Notably, this subjective trend is consistent with our GLCS-based ranking, suggesting that GLCS *aligns well with human preference*. Detailed user study protocol, additional statistics, and further analyses are provided in the *Suppl.*

Qualitative Comparison. As shown by the red arrows in Fig. 6-(a), IMPUS produces relatively natural transitions near the endpoints of the input images, but abrupt changes appear in the middle of the sequence. DiffMorpher tends to lose semantic information from both inputs when the input pair is highly dissimilar (red arrow). FreeMorph generates excessive over-smoothing and color saturation, producing visual characteristics that deviate from the original images (red arrow). In contrast, CHIMERA preserves the semantics of both *A* and *B* while maintaining smooth transitions and perceptually consistent textures. Additional qualitative results are provided in the *Suppl.*, where we also include results for the 16-frame setting.



Fig. 6: Qualitative comparisons with existing methods. (1)–(2) denote the input image pairs. (a)–(d) present results on Morph4Data [5].

5.2 Ablation Studies

Caching Block and Layer Type on ACI. To verify the effectiveness of leveraging all components of diffusion features in ACI, we provide both qualitative and quantitative results in Table 3, Fig. 7, and Fig. 8. As indicated by the red arrows in Fig. 7-(a),(b), using only specific diffusion blocks leads to the loss of meaningful elements from the two inputs (e.g., an arm disappears in the second column) or degradation of fine details (e.g., the fist becomes over-smoothed in the first and second columns). In contrast, using all blocks in Fig. 7-(c) preserves fine details while properly incorporating key elements from both images *A* and

Table 4: Ablation studies on ACI. Left: impact of the injection weight λ_S . Right: effect of Layer- and Timestep-wise Frequency Matching (LTM).

		(a) ACI Ablation – layer weight					(b) ACI Ablation – LTM		
	λ_S	FID _{local} ↓	FID _{global} ↓	LPIPS ↓	PPL ↓	GLCS ↑	LTM	✗	✓
(a)	0.1	<u>178.749</u>	<u>90.525</u>	<u>1.794</u>	<u>0.299</u>	86.236	FID _{local} ↓	182.279	161.054
(b)	0.4 (Ours)	161.054	82.308	1.576	0.263	88.079	FID _{global} ↓	92.8293	82.308
(c)	0.7	186.378	92.275	1.830	0.353	<u>87.888</u>	LPIPS ↓	1.617	1.576
(d)	1.0	222.817	117.846	1.952	0.394	87.599	PPL ↓	0.270	0.263
							GLCS ↑	87.492	88.079

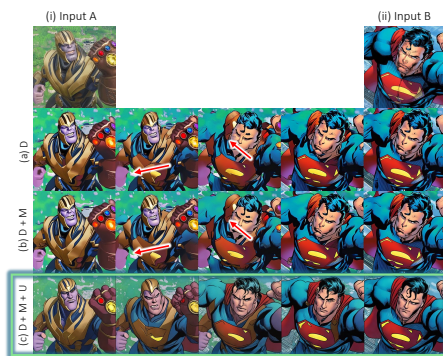


Fig. 7: Qualitative results based on the types of cached block in ACI. (i) and (ii) represent the input image pair, while **D**, **M**, and **U** denote the down, mid, and up block, respectively.



Fig. 8: Qualitative results for different cached layer types in ACI. **KV** denotes the Key and Value features, **Attn** refers to the entire attention layer, and **Res** represents the ResNet layers.

B. This trend is clearly reflected in the left table of Table 3. Similarly, as shown by the red arrows in Fig. 8-(a),(b), when only partial layers are used, insufficient guidance is provided. As a result, important details may disappear (e.g., the horn vanishes in (a)), or unintended objects may be generated (e.g., a cloak-like structure appears in (b)). In contrast, leveraging all layers in Fig. 8-(c) preserves the fine details of both input images and avoids generating unexpected objects. This is also supported by the quantitative results in the right table of Table 3.

Layer- and Timestep-wise Frequency Matching (LTM) of ACI. To validate the effectiveness of LTM, which considers the layer-wise and timestep-wise characteristics of diffusion features, we provide quantitative evaluations in Table 4-(b). As shown in Table 4-(b), applying LTM consistently improves all evaluation metrics compared to the setting without LTM. Without LTM, excessive guidance often introduces noise or injects overly strong details, resulting in unnaturally sharp and unstable structures (see the *Suppl.* for qualitative examples). In contrast, incorporating LTM suppresses such noise and prevents overly emphasized details, leading to more stable and visually consistent results. These experiments support the motivation for applying LTM within ACI.

Caching Injection Weight of ACI. In Table 4-(a), we provide the quantitative evaluation of the injection weight. We set λ_S to 0.4, which achieves the best FID scores. Although the LPIPS and PPL values are relatively higher, we choose $\lambda_S = 0.4$ as the final weight because GLCS offers a more reliable assessment of smoothness. Additional qualitative results are provided in the *Suppl.*

Anchor-correlated Prompt Triplet of SAP.

Table 5 shows the impact of prompt construction for morphing. Row (a) uses independently captioned endpoint prompts following prior work [5,31], which can yield incompatible conditioning for heterogeneous pairs. Replacing them with our anchor-conditioned endpoint prompts (b) yields improvements across all metrics, highlighting the benefit of anchor-conditioned prompt formation. Activating SAP with the shared anchor and the full triplet ($text_{anc}, text_A, text_B$) (c) further improves both fidelity (FID_{local}/FID_{global} , LPIPS) and morphing quality (GLCS) over (b), indicating that an explicit shared anchor-prompt stabilizes intermediate semantics. Finally, CHIMERA (d) combines SAP with ACI and achieves the best overall performance, confirming that semantic anchoring and adaptive cache reuse are complementary.

Table 5: Ablation on anchor-correlated prompt triplet. Independent endpoint prompts, anchor-conditioned endpoint prompts, and the full anchor-correlated prompt triplet are compared.

Method	$FID_{local} \downarrow$	$FID_{global} \downarrow$	LPIPS \downarrow	PPL \downarrow	GLCS \uparrow
(a) Base+per-image prompts	227.558	110.977	1.997	0.316	84.610
(b) Base+paired prompts	<u>205.799</u>	<u>101.291</u>	1.941	0.323	84.598
(c) Base+SAP	209.862	102.401	<u>1.907</u>	<u>0.318</u>	<u>88.076</u>
(d) CHIMERA (Ours)	161.054	82.308	1.576	0.263	88.079

5.3 Further Analysis

Efficiency. To demonstrate the efficiency of CHIMERA, we report computational cost (runtime, TFLOPs, and learnable parameters) in Fig. 1-(c). As shown in Fig. 1-(c), CHIMERA requires significantly lower runtime and TFLOPs than tuning-based models (IMPUS and DiffMorpher). Notably, it is even more efficient than the training-free method FreeMorph.

Backbone-agnostic Applicability. Table 6 shows that CHIMERA consistently improves multiple diffusion backbones (SD 1.4/1.5/2, SDXL, FLUX), indicating broad applicability beyond a specific architecture.

Table 6: Performance comparison across different diffusion backbones.

Exp name	$FID_{local} \downarrow$	$FID_{global} \downarrow$	LPIPS \downarrow	PPL \downarrow	GLCS \uparrow
SD1.4	180.237	91.003	1.782	0.300	86.924
SD1.4 + CHIMERA	176.673	90.593	1.699	0.283	87.311
SD1.5	174.803	89.842	1.724	0.297	86.929
SD1.5 + CHIMERA	172.954	88.914	1.697	0.283	87.037
SD2	187.790	97.053	1.667	0.280	87.741
SD2 + CHIMERA	185.239	95.104	1.659	0.277	88.001
SDXL	209.974	101.715	2.218	0.370	84.809
SDXL + CHIMERA	203.880	100.345	2.156	0.359	84.959
FLUX	167.256	85.326	1.566	0.273	88.253
FLUX + CHIMERA	157.780	80.826	1.552	0.259	89.983

6 Conclusion

We have presented CHIMERA, a zero-shot diffusion-based framework for smooth, semantically coherent, and domain-consistent image morphing. CHIMERA combines Adaptive Cache Injection (ACI) and Semantic Anchor Prompting (SAP) to guide denoising with multi-scale inversion features and VLM-derived anchors, alleviating over-smoothing, over-saturation, and semantic inconsistency in prior

methods. We also introduced GLCS, a morphing-oriented metric that correlates with human judgment. Experiments and a user study show consistent improvements over existing approaches, establishing strong performance for zero-shot diffusion morphing.

Supplementary Material

CHIMERA: Adaptive Cache Injection and Semantic Anchor Prompting for Zero-shot Image Morphing with Morphing-oriented Metrics

Supplementary Contents

- Sec. A Further Analysis on Another Backbone
- Sec. B Qualitative Result of LTM of ACI
- Sec. C Qualitative Result of ACI Injection Weight
- Sec. D Ablation Study on Inversion-Denoising Timestep Mapping (IDM)
- Sec. E Detailed Analyses of SAP
- Sec. F Evaluation Metric
- Sec. G Detail Description of GLCS
- Sec. H User Study: Subjective Preference Analysis
- Sec. I Application
- Sec. J Extended Experiment Results
- Sec. K More Implementation Detail
- Sec. L Additional Qualitative Result
- Sec. M Limitations and Failure Cases

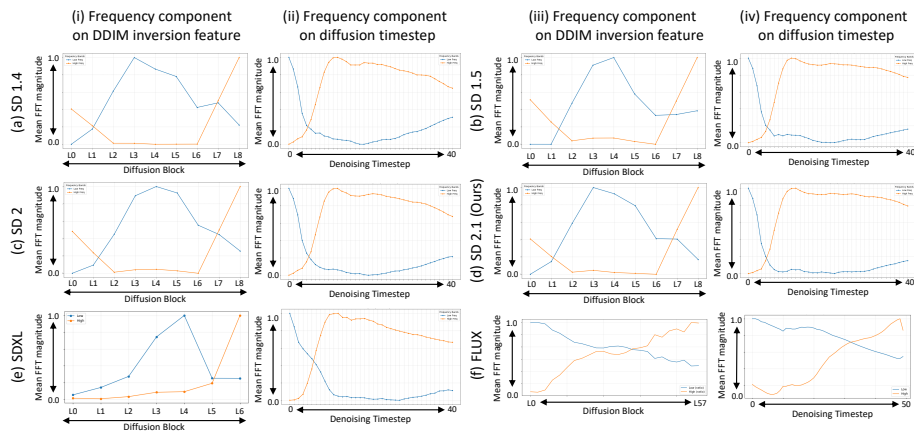


Fig. A: Frequency analysis on another backbone. (i) and (iii) show the layer-wise frequency characteristics of a given diffusion model, while (ii) and (iv) present the timestep-wise frequency characteristics. In each plot, the orange line represents high-frequency components and the blue line represents low-frequency components.

A Further Analysis on Another Backbone

In this section, we provide additional analyses for the experiments presented in Sec. 5.3. In Sec. 3, we analyzed diffusion features from a frequency perspective and presented observations that motivate adaptive feature injection based on layer-wise and timestep-wise characteristics. Here, we extend the same frequency-based analysis to other diffusion models to demonstrate that CHIMERA with ACI can generalize to different architectures.

The analysis in Fig. 3 focuses on layer- and timestep-wise characteristics of SD 2.1 [43]. In this section, we extend the analysis to other U-Net-based diffusion models, including SD 1.4, SD 1.5, and SD 2, as well as larger models such as SDXL [38] and the DiT-based model FLUX [24, 37]. As shown in Fig. A (a)-(c), U-Net-based diffusion models share very similar layer structures and therefore exhibit layer- and timestep-wise characteristics that are largely consistent with those observed in SD 2.1 (Fig. A (d)). Based on this observation, applying CHIMERA leads to consistent performance improvements across these models, as reported in Table 6.

As shown in Fig. A (e), SDXL exhibits frequency characteristics similar to those of SD 2.1, although the number of layers differs from that of SD 2.1. To further demonstrate that CHIMERA is not limited to U-Net-based architectures, we extend the analysis to the diffusion transformer model FLUX (Fig. A (f)). As noted in prior DiT-based studies [6, 60], early layers of DiT mainly capture low-frequency components, while later layers focus on high-frequency details; similarly, early timesteps tend to generate low-frequency structures, while later timesteps refine high-frequency details. These properties are also reflected in Fig. A (f). Based on these observations, applying CHIMERA to both SDXL and FLUX results in consistent performance improvements, as shown in Table 6. These results demonstrate that CHIMERA is not limited to a specific backbone and can be effectively extended to a wide range of diffusion-based models.

B Qualitative Result of LTM of ACI

In this section, we provide qualitative evaluations to demonstrate the effectiveness of LTM, which considers the layer-wise and timestep-wise characteristics of diffusion features. In this experiment, we compare LTM with a baseline that caches and injects all layers at every timestep without applying LTM (w/o LTM). As indicated by the red arrows in Fig. B (a),(c), without LTM, excessive guidance introduces noise or produces overly sharp details. In contrast, when LTM is applied, such noise and excessive details are effectively suppressed by considering both layer-wise and timestep-wise characteristics. Table 4 (b) further supports these observations, showing that applying LTM significantly improves all evaluation metrics.



Fig. B: Qualitative result of LTM.

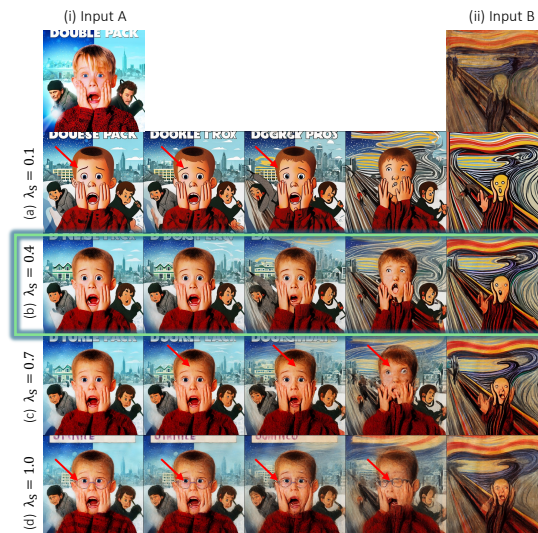


Fig. C: Qualitative results for different injection weights of the cached ACI features in the denoising process. (i) and (ii) denote the input image pair, and (a)–(d) show the results for λ_S values of 0.1, 0.4, 0.7, and 1.0, respectively.

C Qualitative Result of ACI Injection Weight

As shown in Fig. C (a) (red arrow), when the injection weight in ACI is set too small, the results exhibit over-smoothing and saturated colors. This indicates that, without a sufficient ACI effect, the diffusion model tends to produce its characteristic artifacts. In addition, the 2nd, 3rd, and 4th column images in Fig. C (c) (red arrow) become noticeably noisy, and the 1st–4th images in

Table A: Quantitative evaluation with respect to the IDM. We fix the inversion timesteps while performing injections at multiple denoising timesteps.

IDM Ablation - Fixed Inversion Timestep					
	FID _{local} ↓	FID _{global} ↓	LPIPS ↓	PPL ↓	GCSR ↑
(a) Ours	161.054	82.308	1.576	0.263	88.079
(b) Early	<u>186.030</u>	<u>93.002</u>	1.813	0.300	87.784
(c) Mid	196.437	97.327	1.764	0.303	<u>87.929</u>
(d) Late	205.031	101.490	<u>1.726</u>	<u>0.295</u>	87.124

Table B: Quantitative evaluation with respect to the IDM. We fix the denoising timesteps while extracting multiple inversion timesteps.

IDM Ablation - Fixed Denoising Timestep					
	FID _{local} ↓	FID _{global} ↓	LPIPS ↓	PPL ↓	GCSR ↑
(a) Ours	161.054	82.308	1.576	0.263	88.079
(b) Early	<u>195.827</u>	<u>99.192</u>	1.858	0.310	<u>86.036</u>
(c) Mid	204.923	102.100	1.691	0.271	85.306
(d) Late	206.036	102.629	<u>1.690</u>	<u>0.269</u>	85.176

Fig. C (d) (red arrow) generate glasses that do not exist in the input image, while the outputs also appear noisy and blurry. These observations show that when the ACI weight is overly large, the morphing trajectory is excessively constrained, causing high-frequency details that do not exist in the original images to be injected.

D Ablation Study on Inversion-Denoising Timestep Mapping (IDM)

In this section, we present additional experimental results on the effectiveness of the Inversion-Denoising Timestep Mapping (IDM) described in Sec. 4.1. To validate the benefit of IDM, we compare the case where the mapping function is used (Ours) with the case where it is not used, and we report both qualitative and quantitative results. We divide the non-mapping cases into two configurations: (i) the inversion timesteps are fixed to early, mid, or late regions, and the denoising process injects the corresponding fixed cached layers for each timestep; (ii) the inversion timesteps are extracted at all timesteps as in the original setting, but the denoising process injects the cached features only within one fixed region (early, mid, late). For clarity, we unify the interpretation of early, mid, and late as follows: early denotes the state with the least injected noise, mid denotes a medium noise level, and late denotes the highest noise level (although, in practice, early denoising timesteps contain high noise and late timesteps contain almost no noise).

When the inversion timesteps are fixed, Table A shows that our IDM-based model (a) achieves the best quantitative performance. As illustrated in Fig. D, fixing inversion to early, mid, or late produces undesired results: the model generates images that deviate from the input images *A* and *B* (Fig. D (b), (c)), or produces structurally unstable results with severe artifacts (Fig. D (d)). In each case, the red arrows in the figure explicitly indicate the regions where these degradations occur.

When the denoising timesteps are fixed, Table B again shows that the IDM-based model (a) provides the best overall quantitative performance. As shown in Fig. E, injecting cached features only at early, mid, or late denoising timesteps

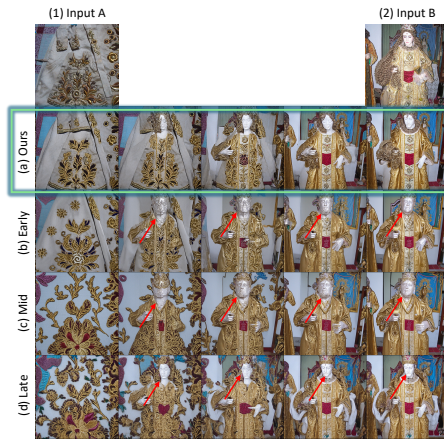


Fig. D: Qualitative results when the inversion timesteps are fixed. Panels (b) Early, (c) Mid, and (d) Late correspond to states with high noise, medium noise, and no noise, respectively. Panel (a) represents our model with the IDM applied.

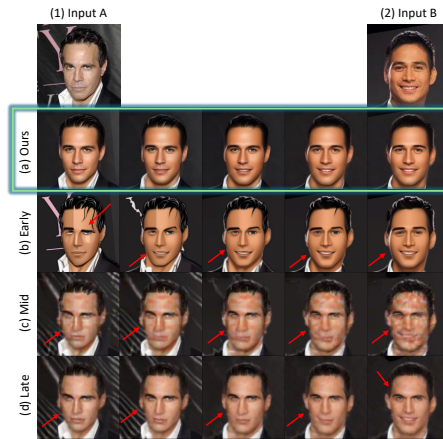


Fig. E: Qualitative results when the denoising timesteps are fixed. Panels (b) Early, (c) Mid, and (d) Late correspond to states with high noise, medium noise, and no noise, respectively. Panel (a) represents our model with the IDM applied.

leads to several issues: overly saturated images (Fig. E (b)) or images that are noticeably blurry or noisy (Fig. E (c), (d)). In these cases, the red arrows explicitly indicate the regions corresponding to the undesired artifacts and noise.






Input A Input B	Text Prompts	
	FreeMorph [ICCV'25]	Ours
	<p>$text_A$: "A young puppy with a pink tongue and a happy expression in a green outdoor setting."</p> <p>$text_B$: "A brown dog with a pink nose and tongue in a room."</p>	<p>$text_A$: "A close-up of a golden puppy with its tongue out, looking cheerful"</p> <p>$text_B$: "A fluffy brown dog with wide eyes and an open mouth, exuding happiness"</p> <p>$text_{anc}$: "Happy dogs with open mouths"</p>
	<p>$text_A$: "A man with white hair and a surprised expression in a dark room."</p> <p>$text_B$: "A cartoon character with spiky hair and a bald head in a car."</p>	<p>$text_A$: "Dr. Emmett Brown and Marty McFly are shocked as they examine the flux capacitor in Back to the Future."</p> <p>$text_B$: "Rick and Morty express surprise during a space journey in Rick and Morty."</p> <p>$text_{anc}$: "Science fiction time travel"</p>
	<p>$text_A$: "A chessboard with a crown and pawns in the center."</p> <p>$text_B$: "A medieval painting depicting a religious scene with a bishop, a king, and a queen."</p>	<p>$text_A$: "A chessboard setup featuring a queen and pawns, symbolizing strategic dominance"</p> <p>$text_B$: "A king receiving a crown from a bishop, signifying the ceremonial bestowment of royal authority"</p> <p>$text_{anc}$: "Monarchical Authority"</p>
	<p>$text_A$: "A man with short brown hair and blue eyes in a black suit."</p> <p>$text_B$: "A woman with brown hair and brown eyes in a portrait."</p>	<p>$text_A$: "Close-up of a man at an event wearing a suit jacket, part of a formal red carpet appearance"</p> <p>$text_B$: "Close-up of a woman with wavy hair, dressed formally, against a neutral background, likely from a photoshoot"</p> <p>$text_{anc}$: "Celebrity portraits with formal attire"</p>
	<p>$text_A$: "A man in a suit holding a red and blue balloon."</p> <p>$text_B$: "A brass compass with a silver needle in a white background."</p>	<p>$text_A$: "A man in a suit holds oversized balloons shaped like numbers, symbolizing precision and scale"</p> <p>$text_B$: "An antique calculating slide rule with a metallic surface and detailed markings represents traditional methods of precise measurement"</p> <p>$text_{anc}$: "Precision in Measurement"</p>

Fig. F: Examples of VLM-generated anchor-correlated prompt triplet. Given two endpoint images, VLM produces a shared anchor-prompt ($text_{anc}$) and the anchor-conditioned endpoint prompts ($text_A$, $text_B$).

E Detailed Analyses of SAP

E.1 VLM instruction strategy

Given two images, we query Qwen2.5-VL [2] with a structured instruction that first asks for a short shared concept (*anchor*) and then asks for endpoint prompts that naturally preserve that shared concept. This anchor-correlated prompt triplet ($text_{anc}$, $text_A$, $text_B$) formulation encourages all prompts to remain mutually correlated, allowing SAP to provide stable semantic guidance during denoising. As shown in Fig. F, the resulting prompt triplet is mutually correlated rather than independently formed. In many cases, this correlation appears through explicit keyword sharing, while in other cases it emerges through higher-level semantic compatibility. This property is important for SAP, since the shared anchor-prompt is intended to guide the denoising process toward se-

mantically coherent intermediate states rather than introducing incompatible endpoint-specific semantics. The full instruction template is provided below.

Prompt template used for Qwen2.5-VL.

You are given two correlated images.

1. Describe their shared visual or semantic theme in one short phrase.
2. Then describe each image separately, but ensure that both captions naturally include that shared theme.

Use this exact format strictly:

Shared theme: [X]

Caption A: [short description of image A including X]

Caption B: [short description of image B including X]

Avoid artistic or stylistic adjectives.

Output format.

Shared theme: [X]

Caption A: [short description of image A including X]

Caption B: [short description of image B including X]

E.2 Anchor reliability

SAP relies on the assumption that the anchor-prompt $text_{anc}$ captures a concept shared by both endpoints. We quantify this property using the cosine similarity ($cossim$) between the anchor-prompt and each endpoint prompt, namely $cossim(text_{anc}, text_A)$ and $cossim(text_{anc}, text_B)$. As shown in Table 1, shared anchors consistently yield higher similarities to both endpoint prompts than deliberately unshared anchors obtained by reversing the correspondence. This observation suggests that $cossim$ serves as a practical proxy for anchor reliability, as semantically relevant anchors remain better aligned with both endpoint prompts.

Motivated by this result, we introduce a $cossim$ -based anchor-reliability criterion for SAP. After generating the anchor-correlated prompt triplet, we encode all prompts using a CLIP text encoder and compute the $cossim$ between the anchor-prompt and each endpoint prompt. If either similarity falls below a predefined threshold, we re-query the VLM until both similarities satisfy the criterion (see Algorithm 1, lines 7–11). In all experiments, we use a threshold of 0.45. This validation step helps ensure that SAP text prompts are constructed from reliable shared anchors and strongly correlated prompt triplets.

E.3 Additional Qualitative Comparisons of Shared vs. Unshared Anchor-prompts

We provide additional qualitative comparisons of shared and intentionally unshared anchors in Fig. G. Consistent with the observation in Fig. 5 (a), shared anchors produce more stable and plausible morphing results, whereas unshared anchors often introduce artifacts. In particular, the red arrows highlight representative failure regions under unshared anchors, such as broken geometric structures, spurious local patterns, and facial artifacts. These examples show

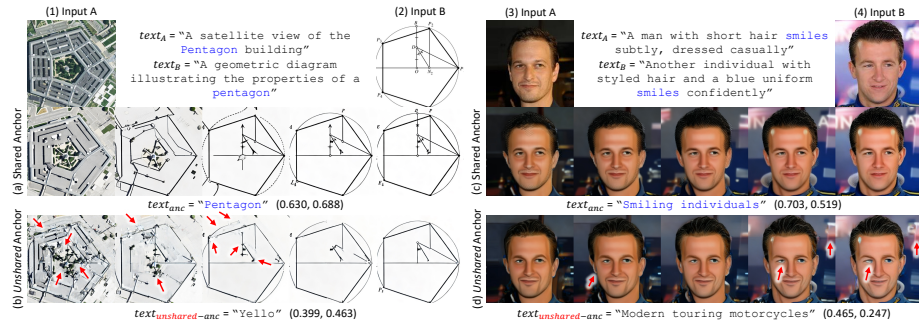


Fig. G: Additional qualitative comparisons of shared and unshared anchors. For each input pair, the upper row ((a), (c)) uses a shared anchor-prompt, while the lower row ((b), (d)) uses an intentionally unshared anchor-prompt. The numbers in parentheses denote the cosine similarity between the anchor-prompt and each endpoint prompt, respectively. Using shared anchors produces smoother morphing results, whereas using unshared anchors leads to distorted structures or localized artifacts.

how unshared anchor guidance can disrupt the semantic compatibility of the morphing even when the endpoint prompts remain individually plausible. This observation is also consistent with the *cossim* analysis. In particular, unshared anchors with low *cossim* tend to produce lower-quality morphing results. Together, these results support our use of *cossim*-based anchor-reliability criterion to filter out unshared anchors or weakly correlated prompt triplets before constructing the text prompts used by SAP.

Table C: Ablation on SAP activation timestep. We compare different SAP schedules, including disabling SAP, applying it only in the early stage (**stage1**), only in the later stage (**stage2**), and throughout both stages. Activating SAP only in the early stage yields the best overall balance across metrics.

Method	FID _{local} ↓	FID _{global} ↓	LPIPS ↓	PPL ↓	GLCS ↑
(a) w/o SAP	163.521	84.669	1.597	0.270	87.811
(b) stage1 (Ours)	161.054	82.308	1.576	0.263	88.079
(c) stage2	193.621	98.564	1.516	0.253	87.624
(d) stage1+stage2	207.917	105.107	1.571	0.262	87.191

E.4 SAP Activation Schedule

Table C shows that restricting SAP to the early stage achieves the best overall performance. Following FreeMorph [5], we divide the denoising timestep into two stages and set the SAP activation schedule accordingly. We define **stage1** as the early timesteps up to 0.2 of the full denoising timestep and **stage2** as the subsequent timesteps from 0.2 to 0.6. Applying SAP only in **stage1** achieves the

best results across all metrics, consistently improving over w/o SAP. In contrast, enabling SAP only in the later stage, or throughout both stages, degrades the overall balance across metrics. These results suggest that SAP is most effective when it provides semantic guidance at the early denoising stage, where the diffusion model establishes the coarse global structure and semantic layout, whereas applying it later can over-constrain the generation process and harm overall morphing quality [22, 29, 35]. We therefore adopt an early-stage-only SAP schedule throughout all experiments.

F Evaluation Metric

This section provides detailed explanations of the metrics introduced in Fig. 5. The motivation, significance, and limitations of these metrics are further discussed in Sec. 4.3.

F.1 Fréchet Inception Distance (FID)-Based Metrics

Local FID. We use a local variant, $\text{FID}_{\text{local}}$, to measure distribution gaps between the input image pair $\{A, B\}$ and the morphing images $\{I_k\}_{k=1}^K$ on a per-pair basis. For an image pair j , the input images $\{A_j, B_j\}$ serve as the real domain, and the morphing images $\{I_k^{(j)}\}_{k=1}^{K_j}$ serve as the generated domain. Let

$$X_{\text{real}}^{(j)} = \{f(A_j), f(B_j)\}, \quad X_{\text{gen}}^{(j)} = \{f(I_k^{(j)})\}_{k=1}^{K_j}. \quad (5)$$

The local FID for pair j is defined as:

$$\text{FID}_{\text{local}}^{(j)} = \text{FID}(\{A_j, B_j\}, \{I_k^{(j)}\}_{k=1}^{K_j}), \quad (6)$$

which measures how well the morphing frames align with the endpoint distribution for each pair. At the dataset level, we compute:

$$\overline{\text{FID}}_{\text{local}} = \frac{1}{N} \sum_{j=1}^N \text{FID}_{\text{local}}^{(j)}, \quad (7)$$

to summarize pair-wise domain consistency.

Global FID. In contrast, $\text{FID}_{\text{global}}$ evaluates the distribution gap at the dataset level. Let

$$\mathcal{X}_{\text{real}} = \bigcup_{j=1}^N \{A_j, B_j\}, \quad \mathcal{X}_{\text{gen}} = \bigcup_{j=1}^N \{I_k^{(j)}\}_{k=1}^{K_j}. \quad (8)$$

We estimate the mean and covariance of each set and apply the standard FID formula:

$$\text{FID}_{\text{global}} = \text{FID}\left(\bigcup_{j=1}^N \{A_j, B_j\}, \bigcup_{j=1}^N \{I_k^{(j)}\}_{k=1}^{K_j}\right), \quad (9)$$

Thus, $\text{FID}_{\text{local}}$ measures pair-wise domain alignment, while $\text{FID}_{\text{global}}$ captures how well the model preserves the distribution of the input images at the dataset level.

F.2 Learned Perceptual Image Patch Similarity (LPIPS)-Based Metrics

LPIPS. For each image pair j , we define an ordered path

$$J_0^{(j)} = A_j, \quad J_k^{(j)} = I_k^{(j)} \quad (k = 1, \dots, K_j), \quad J_{K_j+1}^{(j)} = B_j. \quad (10)$$

We compute pairwise LPIPS distances using $L(\cdot, \cdot)$:

$$d_n^{(j)} = L(J_{n-1}^{(j)}, J_n^{(j)}), \quad n = 1, \dots, K_j + 1. \quad (11)$$

The path-based LPIPS metric is then defined as:

$$\text{LPIPS}^{(j)} = \sum_{n=1}^{K_j+1} d_n^{(j)}, \quad (12)$$

and its dataset-level average is

$$\overline{\text{LPIPS}} = \frac{1}{N} \sum_{j=1}^N \text{LPIPS}^{(j)}. \quad (13)$$

F.3 Perceptual Path Length (PPL)

The Perceptual Path Length (PPL) [20] measures the smoothness of the generator mapping by quantifying how sensitively the generated image changes under small perturbations in the latent space. Given a generator $g : \mathcal{W} \rightarrow \mathcal{Y}$ and two nearby latent codes $\mathbf{w}, \mathbf{w}' \in \mathcal{W}$ sampled along a linear interpolation, the PPL is defined as the expected perceptual distance between the corresponding images, normalized by the squared step size in latent space:

$$\text{PPL} = \mathbb{E}_{\mathbf{w}, \mathbf{w}'} \left[\frac{d_{\text{LPIPS}}(g(\mathbf{w}), g(\mathbf{w}'))}{\|\mathbf{w} - \mathbf{w}'\|_2^2} \right],$$

where $d_{\text{LPIPS}}(\cdot, \cdot)$ denotes the LPIPS perceptual distance computed in a deep feature space. This metric approximates the local curvature of the generator manifold, and lower PPL values indicate a smoother, more semantically consistent latent-to-image mapping.

G Detailed Description of GLCS

Let A and B be the endpoint images, and let $\{I_k\}_{k=1}^K$ be the predicted morphing images ordered from A to B . We adopt a DiffSim-based bounded similarity [50], denoted by

$$s(X, Y) \in [-1, 1], \quad (14)$$

which is implemented as a cosine similarity in a diffusion feature space and primarily captures low-level similarity, unlike LPIPS. In practice, this makes $s(\cdot, \cdot)$ sensitive to both style and semantic correspondence between images.

For each index k , we define the normalized interpolation weight

$$\alpha_k = \frac{k+1}{K+1}, \quad k = 0, \dots, K-1, \quad (15)$$

where α_k encodes the ideal mixing ratio between the two endpoints A and B .

For convenience, we denote the similarities between each frame and the endpoints as

$$s_X(k) = s(X, I_k), \quad X \in \{A, B\}, \quad (16)$$

and introduce a clamping operator to the unit interval,

$$[x]_0^1 = \min(1, \max(0, x)), \quad (17)$$

so that all per-frame consistency terms are normalized to $[0, 1]$.

(i) Global Consistency Score (GCS). We first model the global expected trend of similarities along the morphing sequence. Given the four endpoint similarities

$$s(A, A), s(A, B), s(B, A), s(B, B), \quad (18)$$

we define the expected similarity of frame I_k to each endpoint $X \in \{A, B\}$ using spherical interpolation (`slerp`) in similarity space:

$$\bar{s}_X(k) = \text{slerp}(s(X, A), s(X, B); \alpha_k). \quad (19)$$

Using this expected trend, we define the per-frame global consistency term as

$$g_k = [1 - |s_A(k) - \bar{s}_A(k)|]_0^1 \cdot [1 - |s_B(k) - \bar{s}_B(k)|]_0^1, \quad (20)$$

where each factor evaluates how well the measured similarity $s_X(k)$ matches the expected similarity $\bar{s}_X(k)$ for $X \in \{A, B\}$.

We optionally sharpen the sensitivity of this term by applying an exponent $\gamma \geq 1$,

$$\tilde{g}_k = g_k^\gamma, \quad (21)$$

where $\gamma > 1$ penalizes deviations from the expected trend more strongly.

Finally, we define the Global Consistency Score (GCS) as

$$\text{GCS} = \frac{1}{K} \sum_{k=0}^{K-1} \tilde{g}_k. \quad (22)$$

(ii) **Local Consistency Score (LCS)**. To capture local smoothness along the morphing trajectory, we define a local expectation that relates each frame to its temporal neighbors. For each $X \in \{A, B\}$, we first estimate the locally expected similarity at index k as:

$$\tilde{s}_X(k) = \begin{cases} s_X(1), & k = 0, \\ \frac{1}{2}(s_X(k-1) + s_X(k+1)), & 0 < k < K-1, \\ s_X(K-2), & k = K-1, \end{cases} \quad (23)$$

where boundary images use their single temporal neighbor and interior images use the average of the preceding and succeeding images.

Using $\tilde{s}_X(k)$, we define the per-frame local consistency term as

$$\ell_k = [1 - |s_A(k) - \tilde{s}_A(k)|]_0^1 \cdot [1 - |s_B(k) - \tilde{s}_B(k)|]_0^1, \quad (24)$$

which measures whether the similarity to each endpoint evolves smoothly when compared to neighboring images. The resulting Local Consistency Score (LCS) is given as:

$$\text{LCS} = \frac{1}{K} \sum_{k=1}^K \ell_k. \quad (25)$$

(iii) **Global-Local Consistency Score (GLCS)**. Finally, we combine these two complementary components into our morphing-oriented metric, the **Global-Local Consistency Score (GLCS)**, defined as:

$$\text{GLCS} = \sqrt{\text{GCS} \cdot \text{LCS}}. \quad (26)$$

The full algorithm for GLCS is provided in Algorithm 2.

G.1 Effects of GCS and LCS

Fig. H reports the effect of GCS on selected morphing images. In Fig. H (a) and (b), the red lines and dots indicate cases with low GCS scores, while the blue lines and dots indicate cases with high GCS scores. In Fig. H (a), the Morphing-0 image is highly similar to image A and also shares a similar background with Morphing-1, resulting in a high GCS score of 90.789. In contrast, Morphing-1 should strongly reflect the wolf and moderately reflect the human from image A , but it fails to do so, leading to a low GCS score. Moreover, Morphing-2 does not properly reflect either the wolf or the human, and thus shows the lowest score among the morphing images (Fig. H (b) shows a similar case). Unlike (a) and (b), panels (c) and (d) exhibit consistently high GCS values across the morphing sequence, and human observers also perceive strong domain consistency that includes both domains of A and B . This indicates that (c) and (d) have higher domain consistency than (a) and (b). These results demonstrate that the proposed GCS can evaluate domain consistency in a manner that aligns well with human perception.

Fig. I reports the effect of LCS on selected morphing images. In Fig. I (a) and (b), the red arrows indicate images with low perceptual smoothness, while the blue lines indicate images with high perceptual smoothness. We observe that the LCS score decreases as the difference between adjacent frames increases. In Fig. I (c) and (d), we report transitions where the LCS values are consistently high across the morphing sequence. Human observers also perceive the transitions in (c) and (d) as smoother than those in (a) and (b), and our metric assigns higher scores to these transitions. These results show that the proposed LCS can evaluate perceptual smoothness in a way that is consistent with human judgment.

G.2 Comparison between traditional metrics and GLCS

Fig. J provides a qualitative comparison between FID_{local} and GCS. As shown in Fig. J, the first rows of (a) and (b) achieve better FID_{local} scores than the second rows. However, visual inspection reveals that the third image in the first row of (a) does not properly include both domains of A and B , and the fourth image even produces a result that is unrelated to image B . Similarly, in the first row of (b), the third and fourth images contain almost no elements from image B . These observations indicate that FID_{local} does not align well with human perception when evaluating domain consistency, since it only compares the overall distributions of A, B and the morphing images.

In contrast, the proposed GCS evaluates whether each image properly reflects both domains of A and B according to the interpolation ratio. As a result, the second rows of (a) and (b), which better preserve domain consistency, are assigned higher quality scores than the first rows. This demonstrates that GCS provides a more human-aligned assessment of domain consistency.

Fig. K presents a qualitative comparison between LPIPS, PPL, and LCS. As shown in Fig. K, the first rows of (a) and (b) obtain higher LPIPS and PPL scores than the second rows. However, visual inspection shows that the second rows exhibit smoother transitions than the first rows. This indicates that LPIPS and PPL do not align well with human perception when evaluating smoothness, as they rely on VGG- and GAN-based networks.

In contrast, the proposed LCS leverages DiffSim [50], which measures diffusion-based similarity and benefits from diffusion priors to better match human perception. As a result, LCS assigns higher scores to the second rows in Fig. K (a) and (b), which are perceived as smoother by human observers. These results demonstrate that the proposed LCS provides a perceptually aligned measure of transition smoothness.

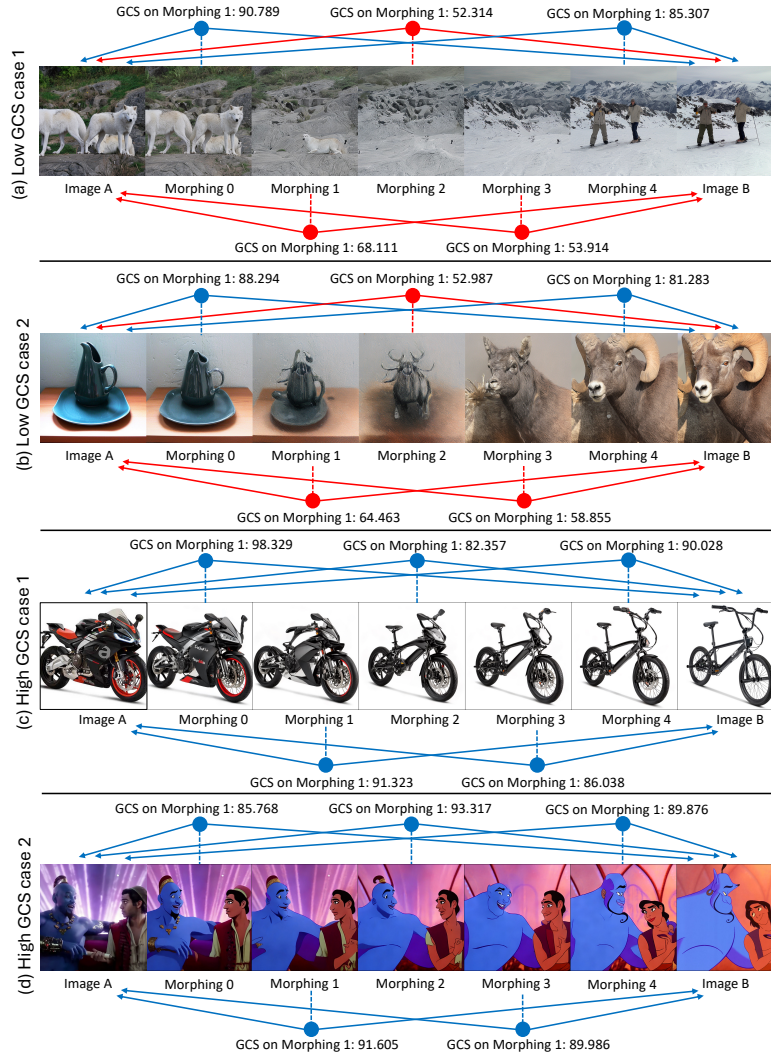


Fig. H: Qualitative examples showing how the GCS component of GLCS aligns with human perception. Blue arrows indicate frames where the domains of A and B are properly mixed according to the perceived interpolation ratio, while red arrows indicate frames where the two domain cues are not well reflected given the same interpolation ratio.

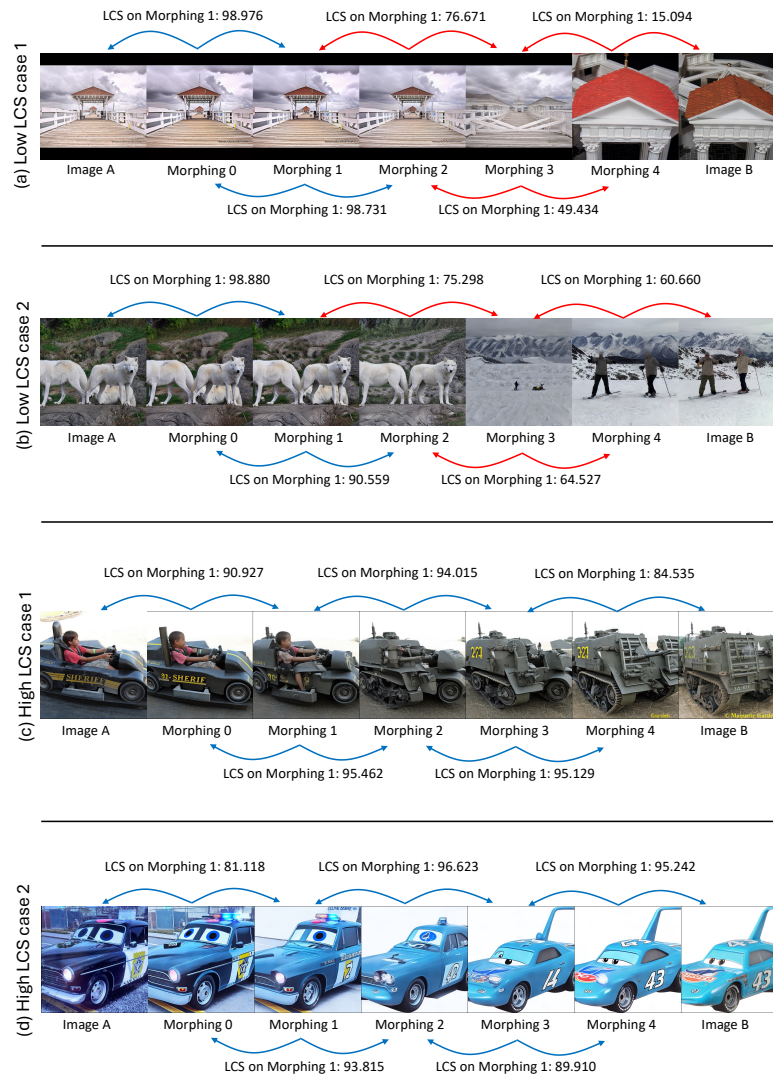


Fig. I: Qualitative examples showing how the LCS component of GLCS aligns with human perception. Blue arrows indicate cases that are judged as similar by human observers, while red arrows indicate cases with abrupt perceptual changes.



Fig. J: Qualitative comparisons between FID_{local} and GCS, which is a component of our proposed metric. Panels (a) and (b) present qualitative results for two different cases.



Fig. K: Qualitative comparisons between LPIPS, PPL, and LCS, which is a component of our proposed metric. Panels (a) and (b) present qualitative results for two different cases.

1-1. Smoothness Score (1 to 5)
 "How smoothly does the transition progress between frames?" Rate each result.

	1 (Very Poor)	2	3	4	5 (Excellent)
Result A	<input type="radio"/>	<input type="radio"/>	<input type="radio"/>	<input type="radio"/>	<input type="radio"/>
Result B	<input type="radio"/>	<input type="radio"/>	<input type="radio"/>	<input type="radio"/>	<input type="radio"/>
Result C	<input type="radio"/>	<input type="radio"/>	<input type="radio"/>	<input type="radio"/>	<input type="radio"/>
Result D	<input type="radio"/>	<input type="radio"/>	<input type="radio"/>	<input type="radio"/>	<input type="radio"/>
Result E	<input type="radio"/>	<input type="radio"/>	<input type="radio"/>	<input type="radio"/>	<input type="radio"/>

Fig. L: User study interface and questionnaire form.

H User Study: Subjective Preference Analysis

H.1 Protocol

We conduct a user study on 15 morphing sequences to assess how well each method aligns with human perception. For each sequence, 36 participants are shown five anonymized results (A – E) generated by CHIMERA, FreeMorph [5], DiffMorpher [62], IMPUS [59], and latent `slerp` (see Fig. L). The mapping between $\{A, \dots, E\}$ and the underlying methods is randomized per sequence and participant. Participants rate each result on a 5-point Likert scale (1–5) for four criteria: Smoothness, Domain Consistency, Perceptual Quality, and Overall Quality.

H.2 Statistical Analyses

Mean Opinion Scores. From the resulting user–sequence–method score matrix, we first aggregate the scores over the 15 sequences for each participant and method, and then compute the mean opinion score (MOS), standard deviation, and average rank (lower is better) for each method and criterion. These statistics are summarized in Table D. CHIMERA achieves the highest MOS, the lowest mean rank, and the highest Borda score across all four criteria. While DiffMorpher shows competitive performance, particularly in Domain Consistency where the MOS gap is the narrowest, CHIMERA still maintains a clear and consistent superiority across all metrics including Smoothness, Perceptual Quality, and Overall Quality. Meanwhile, IMPUS and FreeMorph generally receive lower MOS and worse mean ranks, with `slerp` consistently performing the worst.

Significance Test. To test whether the observed differences are statistically meaningful, we apply a Friedman test over the five methods for each criterion, treating each participant as a block. Table E reports the resulting test statistics and p -values. For all criteria, the null hypothesis that all methods are equivalent is rejected with $p \ll 0.05$, indicating that the differences in participant-level preferences across methods are statistically significant.

Pairwise Preferences. We further analyze pairwise preferences between our CHIMERA and each baseline. For each participant, the scores of CHIMERA and

Table D: Mean opinion scores (MOS), mean rank, and Borda score of each method in the user study. CHIMERA consistently achieves the highest MOS, the best (lowest) mean rank, and the highest Borda score across all four criteria, indicating a strong overall user preference over existing morphing methods.

Criteria	Method	MOS \uparrow	Mean rank \downarrow	Borda score \uparrow
Smoothness	CHIMERA (Ours)	3.828 ± 0.501	1.486	4.514
	FreeMorph [ICCV'25]	2.998 ± 0.472	3.222	2.778
	DiffMorpher [CVPR'24]	3.574 ± 0.481	<u>2.014</u>	<u>3.986</u>
	IMPUS [ICLR'24]	2.815 ± 0.514	3.819	2.181
	slerp	2.243 ± 0.936	4.458	1.542
Domain Consistency	CHIMERA (Ours)	3.661 ± 0.537	1.847	4.153
	FreeMorph [ICCV'25]	2.728 ± 0.612	3.736	2.264
	DiffMorpher [CVPR'24]	3.489 ± 0.511	<u>2.208</u>	<u>3.792</u>
	IMPUS [ICLR'24]	3.172 ± 0.547	2.792	3.208
	slerp	2.326 ± 0.880	4.417	1.583
Perceptual Quality	CHIMERA (Ours)	3.635 ± 0.594	1.819	4.181
	FreeMorph [ICCV'25]	2.957 ± 0.597	3.153	2.847
	DiffMorpher [CVPR'24]	3.383 ± 0.459	<u>2.472</u>	<u>3.528</u>
	IMPUS [ICLR'24]	3.270 ± 0.472	2.694	3.306
	slerp	1.826 ± 0.824	4.861	1.139
Overall Quality	CHIMERA (Ours)	3.639 ± 0.607	1.625	4.375
	FreeMorph [ICCV'25]	2.906 ± 0.519	3.431	2.569
	DiffMorpher [CVPR'24]	3.404 ± 0.448	<u>2.194</u>	<u>3.806</u>
	IMPUS [ICLR'24]	3.067 ± 0.495	2.972	3.028
	slerp	1.913 ± 0.822	4.778	1.222

Table E: Friedman test over the five methods for each subjective criterion. In all cases, the null hypothesis that all methods are equivalent is rejected ($p \ll 0.05$), confirming statistically significant differences in user ratings.

Criteria	Friedman χ^2	p -value
Smoothness	89.251	1.900×10^{-18}
Domain Consistency	66.225	1.420×10^{-13}
Perceptual Quality	76.168	1.128×10^{-15}
Overall Quality	85.354	1.276×10^{-17}

a baseline are first aggregated over the 15 sequences for a given criterion and then compared to count wins (CHIMERA > baseline), ties, and losses. The win-tie-loss statistics in Table F, also visualized in Fig. 1 (b), show that CHIMERA wins the majority of comparisons across all four criteria. Among the baselines, DiffMorpher is the strongest competitor, especially in Domain Consistency, but CHIMERA still maintains a consistent overall advantage across all compared methods.

Relation to GLCS. We further compare the user study outcomes with our GLCS-based quantitative evaluation. Among the four methods for which GLCS is defined (CHIMERA, FreeMorph, DiffMorpher, and IMPUS), CHIMERA attains the highest GLCS on both MorphBench and Morph4Data and, at the same

Table F: Win–tie–loss statistics of CHIMERA against each baseline. For each participant, we aggregate the scores over the 15 sequences for a given criterion and compare the resulting score of CHIMERA with that of each baseline to count wins (CHIMERA > baseline), ties, and losses. CHIMERA wins in the majority of cases, showing consistent subjective superiority. This is also visualized in Fig. 1 (b)

Criteria	Baseline	W / T / L vs. CHIMERA (Ours)
Smoothness	FreeMorph [ICCV’25]	36 / 0 / 0
	DiffMorpher [CVPR’24]	21 / 2 / 13
	IMPUS [ICLR’24]	34 / 1 / 1
	slerp	34 / 0 / 2
Domain Consistency	FreeMorph [ICCV’25]	36 / 0 / 0
	DiffMorpher [CVPR’24]	18 / 2 / 16
	IMPUS [ICLR’24]	26 / 1 / 9
	slerp	32 / 0 / 4
Perceptual Quality	FreeMorph [ICCV’25]	31 / 0 / 5
	DiffMorpher [CVPR’24]	23 / 0 / 13
	IMPUS [ICLR’24]	25 / 1 / 10
	slerp	35 / 0 / 1
Overall Quality	FreeMorph [ICCV’25]	35 / 0 / 1
	DiffMorpher [CVPR’24]	21 / 2 / 13
	IMPUS [ICLR’24]	29 / 1 / 6
	slerp	35 / 0 / 1

time, achieves the highest Overall Quality MOS, the best mean rank, and the highest Borda score in Table D. Methods with lower GLCS values also tend to receive lower MOS and worse ranks in the user study, indicating that GLCS is aligned with human preference at the method level. Given this agreement between human judgments and dataset-level scores, we regard GLCS as a promising reference metric for future image morphing research, providing a principled quantitative measure that jointly reflects temporal smoothness and semantic consistency.

I Application

I.1 Video Frame Interpolation

Although CHIMERA is designed for still-image morphing, its capability to generate temporally dense sequences naturally suggests an application to video frame interpolation (VFI). To probe this connection, frames from VFI benchmark datasets [39, 58] are used as input, where two frames separated by a fixed temporal offset are treated as endpoints and the intermediate outputs of CHIMERA are interpreted as interpolated results. As shown in Fig. M on Vimeo90K-septuplet [58] some frames visually resemble reasonable interpolation, but noticeable artifacts remain. In the CHIMERA rows ((d), (d’)), the red arrows highlight typical failure modes such as truncated or duplicated limbs and locally distorted arm configurations. Similar issues are also observed in the other morphing baselines. IMPUS [59] (rows (a), (a’)) often produces implausible hand

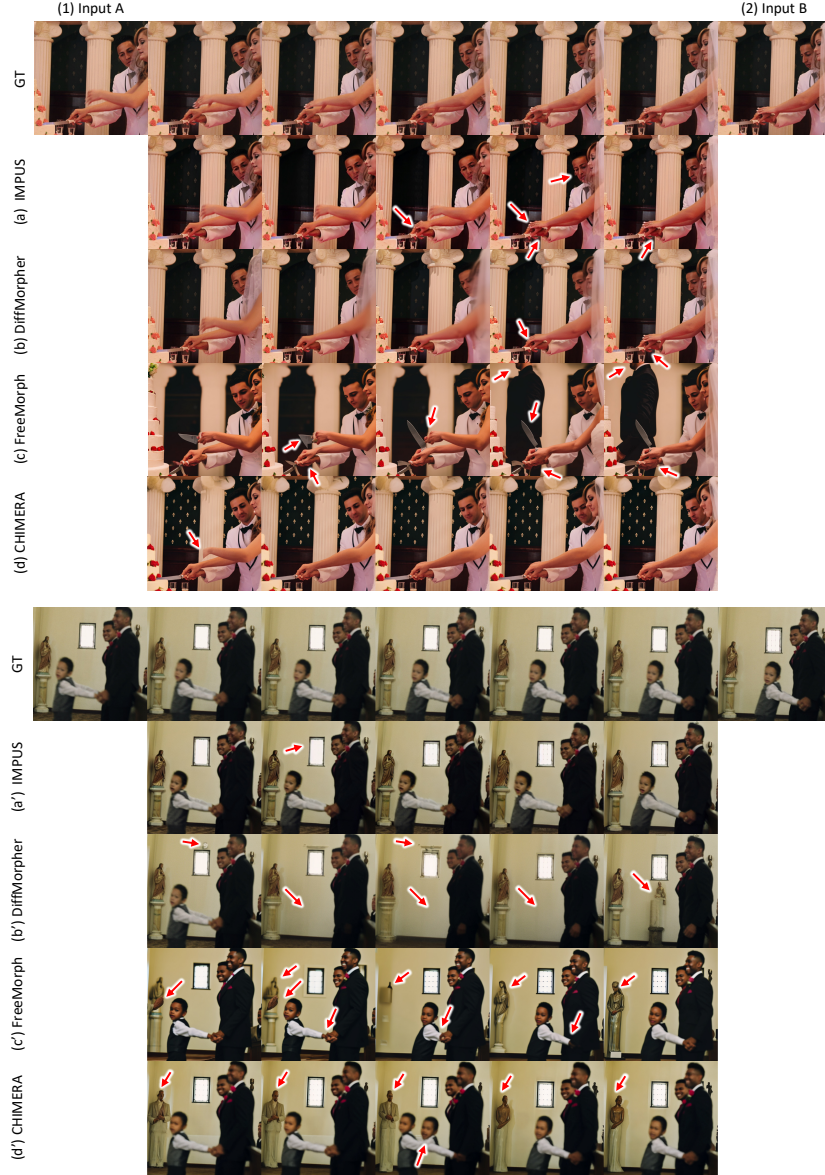


Fig. M: Qualitative VFI results on Vimeo90K-septuplet. Panels (a)–(d) and (a')–(d') correspond to IMPUS, DiffMorpher, FreeMorph, and CHIMERA (Ours), respectively. For each sequence, red arrows mark representative artifacts such as unrealistic limb configurations or duplicated local structures in the interpolated frames.

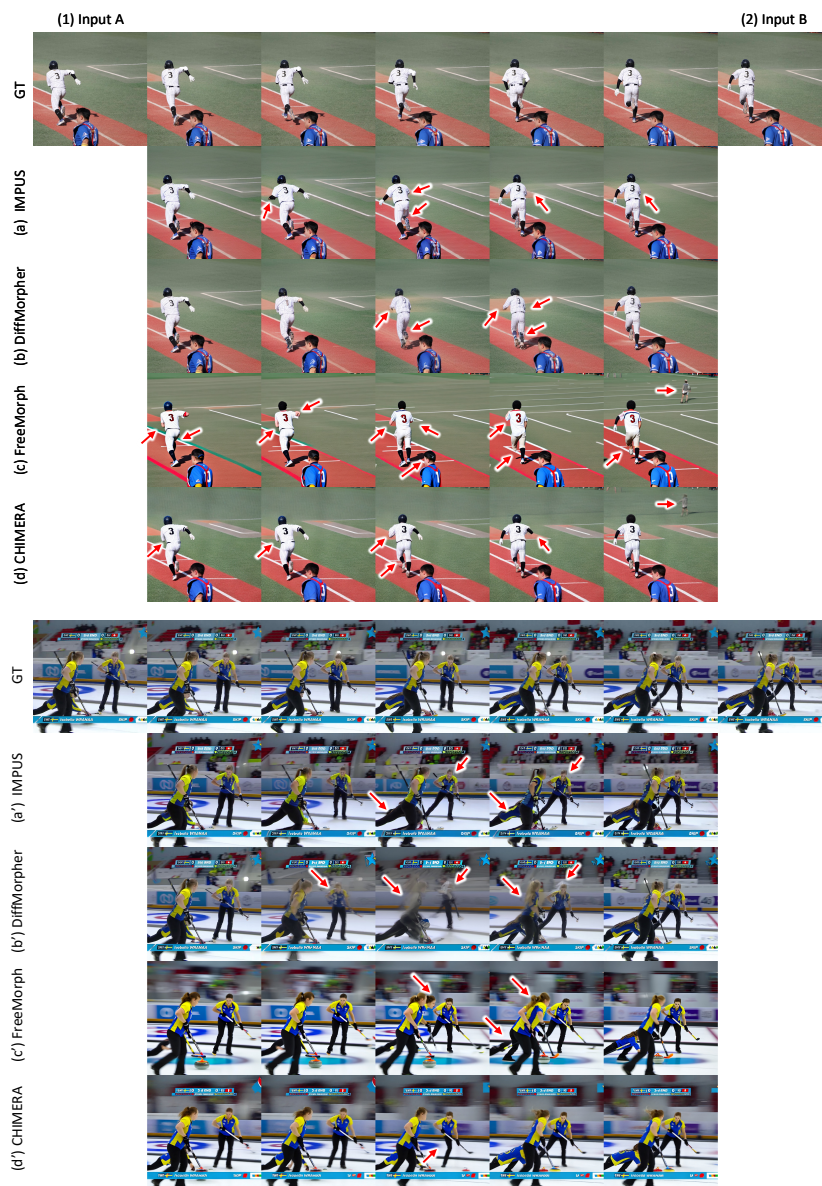


Fig. N: Qualitative VFI results on DAVIS. Panels (a)–(d) and (a')–(d') correspond to IMPUS, DiffMorpher, FreeMorph, and CHIMERA (Ours), respectively. The red arrows highlight severe failure cases where the interpolated results exhibit non-physical human bodies, including truncated or distorted arms and legs.

shapes or causes arms to partially disappear mid sequence. DiffMorpher [62] (rows (b), (b')) yields over-smoothed and blurry frames consistent with its morphing behavior, and FreeMorph [5] (rows (c), (c')) hallucinates content absent from both inputs (e.g., transforming a statue into a realistic human).

On the DAVIS dataset [39] in Fig. N, where human motion and occlusions are more complex, all morphing methods exhibit pronounced non-physical deformations. CHIMERA (rows (d), (d')) generates unrealistic human bodies with truncated or severely warped arms and legs, and sometimes stretches limbs into unnatural shapes across frames. IMPUS (rows (a), (a')) produces broken silhouettes with missing or dislocated arms, while DiffMorpher (rows (b), (b')) shows similar limb truncation together with strong motion blur that obscures fine details. FreeMorph (rows (c), (c')) suffers from distorted body shapes and over-saturated colors and, like CHIMERA, sometimes hallucinates entirely new objects in the background. Overall, these observations indicate that such failures are not specific to our method but are inherent to morphing methods when applied to VFI data.

We conjecture that this stems from a fundamental mismatch between the objectives of morphing and VFI. Unlike VFI methods that establish explicit correspondences between input frames and reconstruct the motion trajectory connecting them through optical flow [34], deformable kernels [11], or learned spatiotemporal representations [23, 65], morphing models operate as generative processes that synthesize plausible in between states without being constrained to follow the true motion path. CHIMERA has no motion specific modules and receives no supervision from real videos; it is optimized for smooth transitions between two inputs rather than faithful reconstruction of motion trajectories. Moreover, CHIMERA is applied to VFI datasets in a purely zero-shot setting without domain specific fine-tuning, further widening the gap relative to VFI models. As a result, intermediate frames can traverse “imagined” states in latent space that do not correspond to physically realizable frames, which is acceptable or even desirable in morphing contexts but manifests as artifacts in VFI benchmarks.

Overall, these observations indicate that CHIMERA is distinct from reconstruction-driven VFI methods. They also suggest a natural extension: augmenting the cache and prompt-based design with explicit motion priors [28, 46, 54] and video-driven objectives [8, 57] could evolve the framework toward a VFI model that better satisfies the physical and temporal requirements of standard benchmarks.

I.2 Creative Content Creation and Animation

CHIMERA directly supports applications in film, game, and animation production, where artists often require smooth transitions between disparate visual concepts [51]. Given two images that serve as keyframes, the framework generates a temporally dense sequence of structurally consistent and semantically coherent intermediate frames without manual correspondence annotation or model fine-tuning. This capability aligns with the growing demand for engaging transitions

in short-form video platforms (e.g., TikTok, Kuaishou), where visually distinctive morphing effects contribute to viewer engagement and content memorability. By providing zero-shot generation of high-quality metamorphic transitions, CHIMERA lowers the barrier for both professional creators and non-experts to prototype and deploy production-ready visual effects, ranging from character evolution and object transformations to stylized scene changes tailored for short-form content.

J Extended Experiment Results

Table G: Quantitative results of 14 frame morphing on Morph4Data and MorphBench datasets. The best scores are marked in bold, while the second best are underlined.

Morph4Data						MorphBench					
Model name	FID _{local} ↓	FID _{global} ↓	LPIPS ↓	PPL ↓	GLCS ↑	Model name	FID _{local} ↓	FID _{global} ↓	LPIPS ↓	PPL ↓	GLCS ↑
IMPUS	120.815	60.046	2.737	0.183	88.944	IMPUS	78.944	40.892	1.587	0.106	93.679
DiffMorpher	175.409	89.870	<u>1.875</u>	<u>0.125</u>	89.212	DiffMorpher	<u>90.739</u>	<u>46.176</u>	1.051	0.070	<u>94.814</u>
FreeMorph	178.792	94.062	2.538	0.169	<u>90.151</u>	FreeMorph	141.727	79.178	1.776	0.118	92.412
CHIMERA	<u>151.359</u>	<u>78.569</u>	1.846	0.123	91.888	CHIMERA	111.496	61.401	<u>1.141</u>	<u>0.076</u>	95.593

This section provides additional quantitative and qualitative evaluations that supplement Sec. 5.1. In Sec. J.1, we present qualitative and quantitative results for the setting where 14 morphing images are generated between input images A and B . Unlike Sec. 5.1, which reports quantitative results for the 5-image morphing setting, this section evaluates CHIMERA under a longer morphing transition to assess the general applicability of the proposed method. In addition, Sec. J.2 provides further qualitative results for the 5-frame morphing scenario discussed in Sec. 5.1.

J.1 Extended Evaluation on Challenging 14-Image Morphing

Table G reports the quantitative results for the setting where 14 morphing images are generated between each input image pair. Similar to the observations in Sec. 5.1, IMPUS achieves the best scores in FID_{local} and FID_{global} on both datasets, but shows weaker performance in LPIPS, PPL, and GLCS. DiffMorpher obtains the best LPIPS and PPL scores, yet its performance in FID_{local}, FID_{global}, and GLCS is relatively lower. FreeMorph shows degraded performance in all metrics except GLCS.

In contrast, the proposed CHIMERA demonstrates performance comparable to the fine-tuning-based models IMPUS and DiffMorpher across FID_{local}, FID_{global}, LPIPS, and PPL, while achieving a significantly higher GLCS. Furthermore, compared to FreeMorph, which is also a zero-shot model, CHIMERA outperforms it by a large margin across all metrics.

Qualitatively, IMPUS maintains strong domain consistency in each generated image but lacks smooth transitions between frames. DiffMorpher produces smooth transitions but often introduces severe artifacts, leading to poor domain consistency. FreeMorph provides visually smooth transitions but suffers from overly saturated colors, which also reduces domain consistency. In contrast, CHIMERA achieves both smooth frame-to-frame transitions and strong domain consistency, making it superior across both qualitative and quantitative evaluations.

We additionally provide qualitative results for the setting with 14 morphing images in Fig. Q and Fig. R. Similar to Fig. O and Fig. P, IMPUS shows transitions with insufficient smoothness, while DiffMorpher contains many frames where the structure collapses. FreeMorph also produces images with overly saturated colors. In contrast, as shown in panels (d) and (h) of Fig. Q and Fig. R, CHIMERA consistently maintains both smooth transitions and strong domain consistency.

These qualitative results are consistent with the quantitative evaluations presented earlier. For example, IMPUS achieves high scores in FID_{local} and FID_{global} , which measure domain consistency, but shows lower performance in LPIPS and PPL, which assess smoothness. Conversely, DiffMorpher performs well in terms of smoothness but exhibits lower domain consistency.

J.2 Additional Qualitative Result on 5-Image Morphing

Fig. O and Fig. P present qualitative results for the setting where five morphing images are generated between A and B . As shown in panels (a) and (e) of Fig. O and Fig. P (red arrows), IMPUS produces frames with abrupt transitions. In panels (b) and (f), the morphing images exhibit good smoothness, but the red arrows highlight collapsed structures or noticeable artifacts. In panels (c) and (g), the transitions remain smooth, yet the red arrows indicate a tendency toward excessively saturated colors. In contrast, panels (d) and (h) of Fig. O and Fig. P show that the proposed CHIMERA preserves both domain consistency and smoothness.

K More Implementation Detail

All experiments on Morph4Data [5] and MorphBench [62] are conducted at a resolution of 768×768 . For SD 1.4, SD 1.5, SD 2, and SDXL [38], we use the same DDIM sampler as in the SD 2.1 setting of CHIMERA. For FLUX [24], we use the default Euler-based ODE sampler provided by the Flow Matching framework. For SD 1.4, SD 1.5, SD 2, and SDXL, we use a total of 40 timesteps, while for FLUX we follow the commonly used default setting of 50 steps. All configurations related to ACI and SAP remain identical to those used in the SD 2.1 setting of CHIMERA. All experiments are conducted on a single NVIDIA RTX 5090 GPU, except for FLUX, which is evaluated on a single NVIDIA RTX Pro 6000 GPU due to its larger model size.



Fig. O: First qualitative comparison showing the results of generating five morphing images between input images A and B . Panels (1)–(4) denote the input images, and panels (a)–(d) correspond to IMPUS, DiffMorpher, FreeMorph, and CHIMERA (Ours), respectively. The same convention applies to panels (e)–(h).

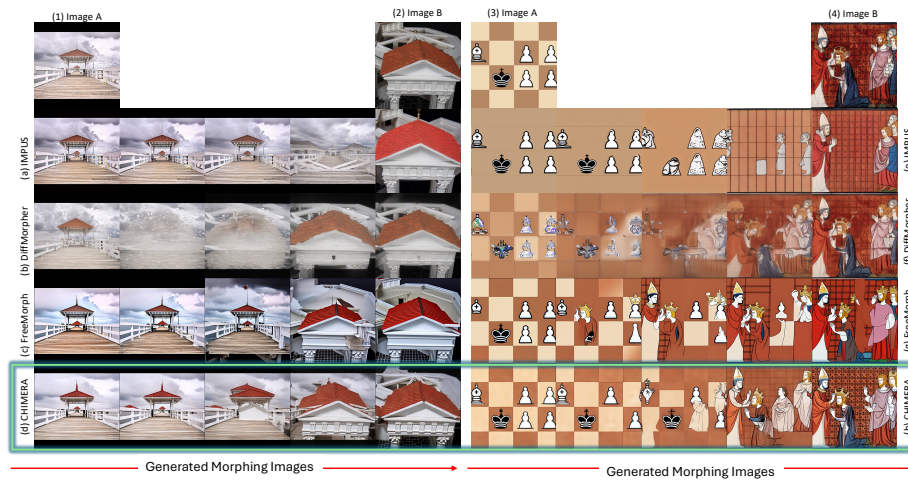


Fig. P: Second qualitative comparison showing the results of generating five morphing images between input images A and B . Panels (1)–(4) denote the input images, and panels (a)–(d) correspond to IMPUS, DiffMorpher, FreeMorph, and CHIMERA (Ours), respectively. The same convention applies to panels (e)–(h).

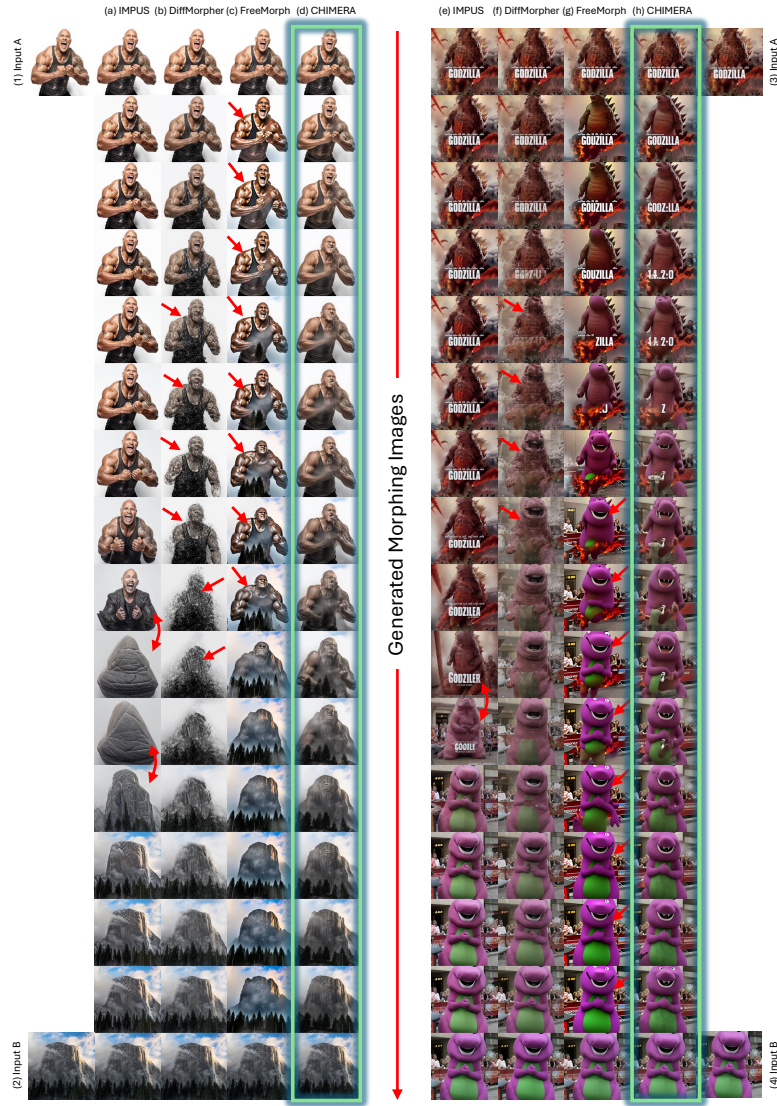


Fig. Q: First qualitative comparison showing the results of challenging 14-image morphing (compared to 5-image morphing) between input images *A* and *B*. Panels (1)–(4) denote the input images, and panels (a)–(d) correspond to IMPUS, DiffMorpher, FreeMorph, and CHIMERA (Ours), respectively. The same convention applies to panels (e)–(h). Please zoom in for better visualization.

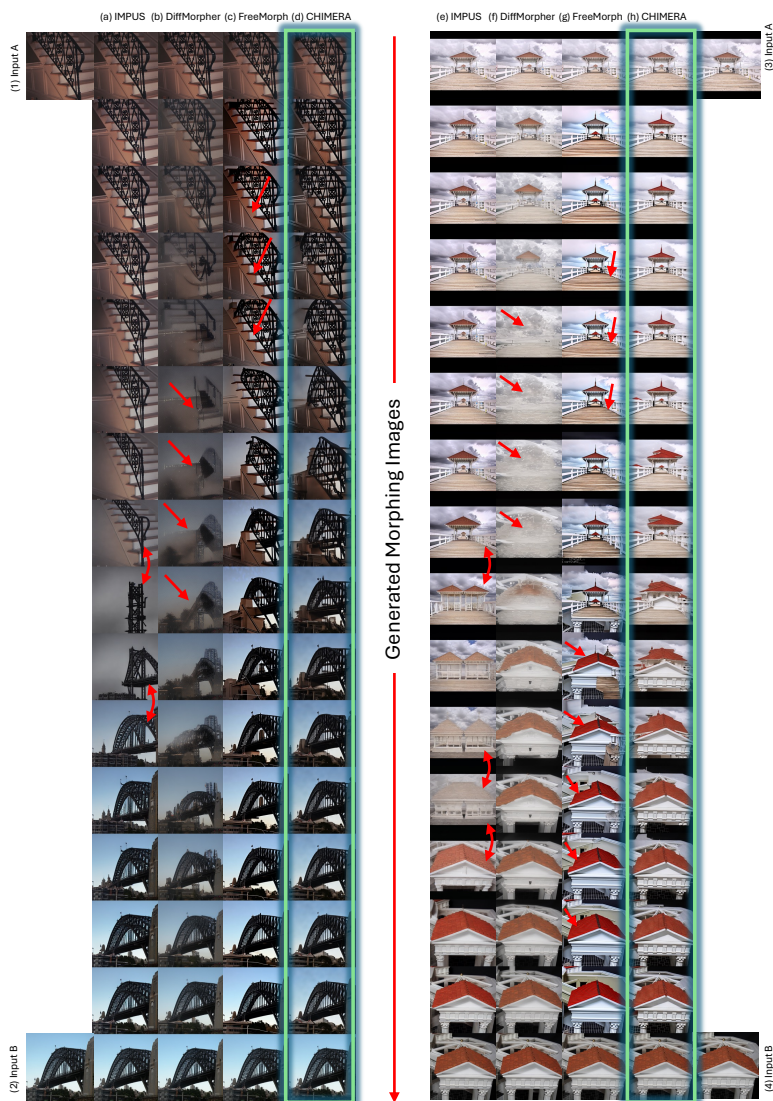


Fig. R: Second qualitative comparison showing the results of challenging 14-image morphing (compared to 5-image morphing) between input images A and B . Panels (1)–(4) denote the input images, and panels (a)–(d) correspond to IMPUS, DiffMorpher, FreeMorph, and CHIMERA (Ours), respectively. The same convention applies to panels (e)–(h). Please zoom in for better visualization.

L Additional Qualitative Result

In this section, we present additional qualitative comparisons for the 5-frame and 14-frame morphing scenarios.



Fig. S: Additional qualitative results for 5-frame morphing.

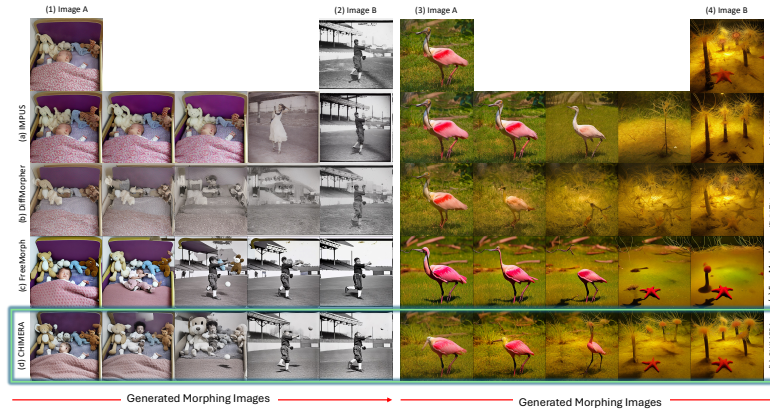


Fig. T: Additional qualitative results for 5-frame morphing.

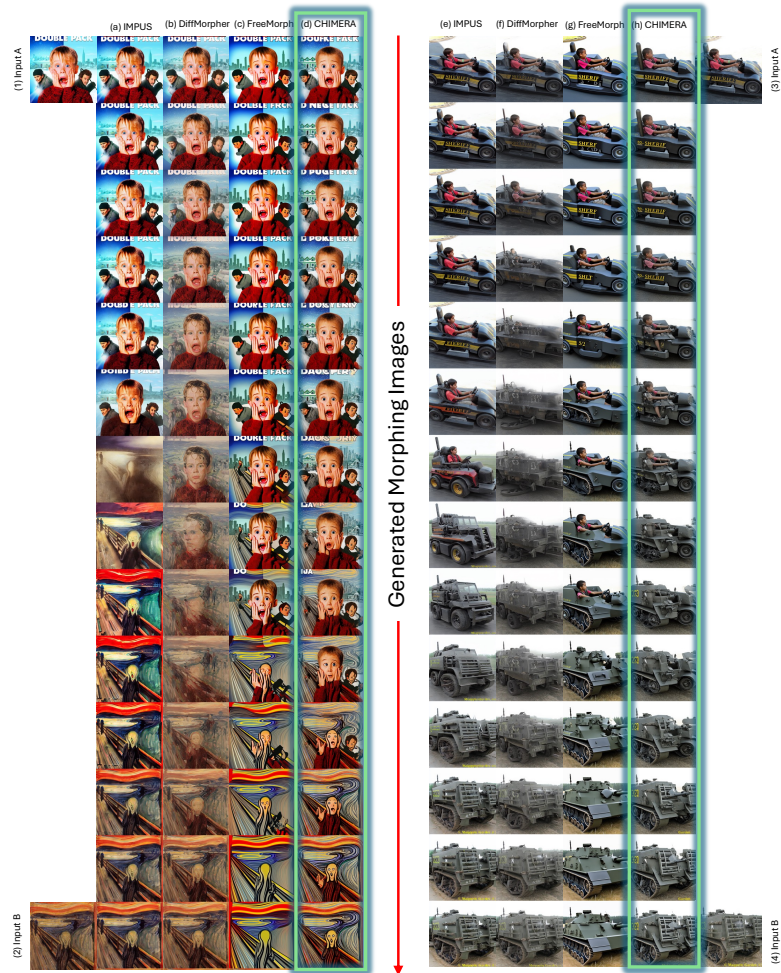


Fig. U: Additional qualitative results for 14-frame morphing.



Fig. V: Additional qualitative results for 14-frame morphing.

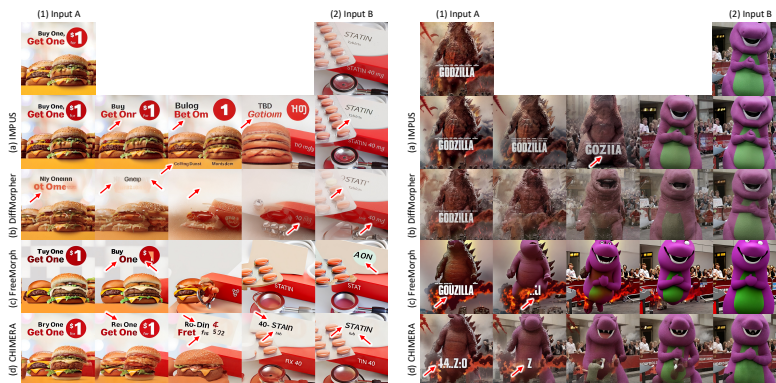


Fig. W: Failure cases on images with prominent text. When the endpoint images contain different words or textual layouts, all compared methods, including CHIMERA, often produce broken or unreadable characters and occasional abrupt changes in the rendered text.

M Limitations and Failure Cases

Text Rendering and Typography. Although CHIMERA produces smooth and semantically coherent transitions in general scenes, it remains limited when the endpoint images contain prominent textual elements, such as logos, signage, or dense typography (see Fig. W). In such cases, the generated intermediates often exhibit temporally inconsistent, partially broken, or illegible characters, even when the surrounding scene structure remains relatively coherent. Importantly, this limitation is not unique to CHIMERA, but is consistently observed across other diffusion-based morphing methods as well [5, 59, 62].

This failure is largely due to the inherent limitations of the underlying pre-trained diffusion backbones rather than to the morphing mechanism itself [9, 43]. Existing text-to-image diffusion models are well known to treat text as a high-frequency visual pattern rather than as a structured symbolic entity, and therefore often lack the fine-grained control required for accurate glyph generation [14, 61, 66]. Since CHIMERA operates within such a pre-trained latent space, it inevitably inherits these weaknesses in text rendering, which explains why typographic failures persist even when the global morphing remains smooth.

Future Direction: Glyph-Aware Morphing. We view this limitation as a meaningful direction for future research. Addressing textual inconsistency likely requires going beyond standard attention-based composition and incorporating explicit text-control mechanisms developed for recent text generation and editing frameworks, such as layout-guided generation [66] or OCR-consistency objectives [9]. A promising next step is a *glyph-aware morphing* framework that explicitly separates textual content from appearance, enabling smooth interpolation of character geometry while preserving legibility. Extending our current attention composition strategy to better preserve glyph structure may provide an effective path toward bridging semantic morphing and precise typographic control.

Algorithm 1 CHIMERA

Input: input image pair A, B ; number of morphing images K ; DDIM inversion steps N_{inv} ; denoising steps N_{dng} ; layer groups $\mathcal{S} = \{D, M, U\}$; ACI weights $\{\lambda_S\}_{S \in \mathcal{S}}$; SAP active ratio η ; anchor-reliability threshold ρ_{thr} ;
Output: morphing sequence $\{I_k\}_{k=0}^{K-1}$.

Step 1: DDIM inversion and cache collection.

- 1: For each $X \in \{A, B\}$, run DDIM inversion to obtain the inverted latent z_X and cached multi-scale U-Net features $H_S(X, t)$ for $S \in \mathcal{S}$ and $t \in \mathcal{T}_{\text{inv}}$ as in Eq. (1).

Step 2: Layer- and Timestep-wise Frequency Matching (LTM).

- 2: For each cached feature tensor Z , compute its FFT-magnitude descriptor $r(Z) = \text{Pool}\left(\frac{1}{C} \sum_{c=1}^C |\mathcal{F}(Z_c)|\right)$.
- 3: Construct layer-group prototypes \bar{r}_S and timestep prototypes \bar{r}_t , compute $D_{S,t} = d(\bar{r}_S, \bar{r}_t)$, and assign the matched group $S^*(t) = \arg \min_{S \in \mathcal{S}} D_{S,t}$.
- 4: Re-organize cached features using the matched group, i.e., use $H_{S^*}(X, t)$ for subsequent interpolation and injection.

Step 3: Morphing latent construction and cache interpolation.

- 5: For $k = 0, \dots, K-1$, compute α_k and construct the morphing latent $z_k = \text{slerp}(z_A, z_B; \alpha_k)$.
- 6: For each k and $t \in \mathcal{T}_{\text{inv}}$, construct the interpolated cache $\widehat{C}_{S^*}(k, t) = \text{slerp}(H_{S^*}(A, t), H_{S^*}(B, t); \alpha_k)$ as in Eq. (2).

Step 4: Anchor-correlated prompt triplet construction for SAP.

- 7: Initialize $\rho \leftarrow 0$.
- 8: **while** $\rho < \rho_{\text{thr}}$ **do**
- 9: Query the VLM with (A, B) to obtain $(\text{text}_{\text{anc}}, \text{text}_A, \text{text}_B)$, and encode them into $(e_{\text{anc}}, e_A, e_B)$.
- 10: Compute anchor reliability $\rho = \min(\text{cossim}(e_{\text{anc}}, e_A), \text{cossim}(e_{\text{anc}}, e_B))$.
- 11: **end while**

Step 5: Denoising with IDM, ACI, and SAP.

- 12: For each morphing index $k = 0, \dots, K-1$, initialize $x_{\tau_0}^{(k)} \leftarrow z_k$.
- 13: **for** each denoising timestep $\tau \in \mathcal{T}_{\text{dng}}$ **do**
- 14: Map τ to the inversion timestep $t \leftarrow \phi(\tau)$ via IDM, and run the diffusion U-Net on $x_{\tau}^{(k)}$ to obtain $\{F_S^{(\tau)}\}_{S \in \mathcal{S}}$.
- 15: For each $S \in \mathcal{S}$, retrieve $\widehat{C}_{S^*}(k, \phi(\tau))$ and compute the ACI feature $\widetilde{F}_S^{(\tau)} = F_S^{(\tau)} + \lambda_S \cdot \widehat{C}_{S^*}(k, \phi(\tau))$.
- 16: **if** $\tau \in \mathcal{T}_{\text{dng}}^{\text{early}}(\eta)$ **then** apply SAP-guided cross-attention as in Eq. (4); **else** use the original cross-attention.
- 17: Update the latent by one denoising step to obtain $x_{\tau+1}^{(k)}$.
- 18: **end for**
- 19: Decode $x_{\tau_{\text{final}}}^{(k)}$ with the VAE decoder to obtain $I_k = \text{VAE}^{-1}(x_{\tau_{\text{final}}}^{(k)})$.
- 20: **end for**

Step 6: Return.

- 21: **return** morphing sequence $\{I_k\}_{k=0}^{K-1}$.
-

Algorithm 2 Global–Local Consistency Score (GLCS)

Input: endpoint images A, B ; morphing images $\{I_k\}_{k=1}^K$; DiffSim-based bounded similarity $s(\cdot, \cdot) \in [-1, 1]$; sharpening exponent $\gamma \geq 1$.

Output: Global Consistency Score GCS, Local Consistency Score LCS, and Global–Local Consistency Score GLCS.

Step 1: Similarity computation.

- 1: **for** each endpoint $X \in \{A, B\}$ **do**
- 2: **for** $k = 1, \dots, K$ **do** compute the per-frame similarity $s_X(k) = s(X, I_k)$.
- 3: **end for**
- 4: **end for**
- 5: Compute the four endpoint similarities $s(A, A)$, $s(A, B)$, $s(B, A)$, and $s(B, B)$.

Step 2: Global Consistency Score (GCS).

- 6: **for** $k = 1, \dots, K$ **do**
- 7: Compute the normalized interpolation ratio $\alpha_k = \frac{k}{K+1}$.
- 8: Estimate the globally expected similarities by spherical interpolation in similarity space: $\bar{s}_A(k) = \text{slerp}(s(A, A), s(A, B); \alpha_k)$ and $\bar{s}_B(k) = \text{slerp}(s(B, A), s(B, B); \alpha_k)$.
- 9: Compute the per-frame global consistency $g_k = [1 - |s_A(k) - \bar{s}_A(k)|]_0^1 \cdot [1 - |s_B(k) - \bar{s}_B(k)|]_0^1$, where $[x]_0^1 = \min(1, \max(0, x))$.
- 10: Sharpen the global term by $\tilde{g}_k = g_k^\gamma$.
- 11: **end for**
- 12: Aggregate all sharpened terms: $\text{GCS} = \frac{1}{K} \sum_{k=1}^K \tilde{g}_k$.

Step 3: Local Consistency Score (LCS).

- 13: **for** $k = 1, \dots, K$ **do**
- 14: For each endpoint $X \in \{A, B\}$, estimate the locally expected similarity $\tilde{s}_X(k)$ from neighboring frames: use the single adjacent frame at the boundaries and the average of the previous and next frames otherwise.
- 15: Compute the per-frame local consistency $\ell_k = [1 - |s_A(k) - \tilde{s}_A(k)|]_0^1 \cdot [1 - |s_B(k) - \tilde{s}_B(k)|]_0^1$.
- 16: **end for**
- 17: Aggregate all local consistency terms: $\text{LCS} = \frac{1}{K} \sum_{k=1}^K \ell_k$.

Step 4: Global–Local Consistency Score (GLCS).

- 18: Combine the two scores by geometric mean: $\text{GLCS} = \sqrt{\text{GCS} \cdot \text{LCS}}$.

- 19: **return** GCS, LCS, GLCS.
-

References

1. Aloraibi, A.Q.: Image morphing techniques: A review. *Technium* **9** (2023)
2. Bai, S., Chen, K., Liu, X., Wang, J., Ge, W., Song, S., Dang, K., Wang, P., Wang, S., Tang, J., et al.: Qwen2. 5-vl technical report. arXiv preprint arXiv:2502.13923 (2025)
3. Beier, T., Neely, S.: Feature-based image metamorphosis. *ACM SIGGRAPH Computer Graphics* **26**(2), 35–42 (1992)
4. Brack, M., Friedrich, F., Hintersdorf, D., Struppek, L., Schramowski, P., Kersting, K.: Sega: Instructing text-to-image models using semantic guidance. *Advances in Neural Information Processing Systems* **36**, 25365–25389 (2023)
5. Cao, J., Lin, X., Xu, Y., Xu, J., Zhang, Z., Li, Z.: Freemorph: Tuning-free generalized image morphing with diffusion models. *Proceedings of the IEEE/CVF Conference on Computer Vision and Pattern Recognition (CVPR)* (2025)
6. Chang, S., WANG, P., Tang, J., Wang, F., Yang, Y.: Sparsedit: Token sparsification for efficient diffusion transformer. In: *The Thirty-ninth Annual Conference on Neural Information Processing Systems* (2025), <https://openreview.net/forum?id=jTBxyQempF>
7. Chefer, H., Mokady, R., Lang, O., Alaluf, Y., Chechik, G., Cohen-Or, D.: Attention interpolation for text-to-image diffusion models. *Proceedings of the IEEE/CVF International Conference on Computer Vision (ICCV)* (2023)
8. Chen, J., Feng, B.Y., Cai, H., Wang, T., Burner, L., Yuan, D., Fermuller, C., Metzler, C.A., Aloimonos, Y.: Repurposing pre-trained video diffusion models for event-based video interpolation. In: *Proceedings of the Computer Vision and Pattern Recognition Conference*. pp. 12456–12466 (2025)
9. Chen, J., Huang, Y., Lv, T., Cui, L., Chen, Q., Wei, F.: Textdiffuser: Diffusion models as text painters. *Advances in Neural Information Processing Systems* **36**, 9353–9387 (2023)
10. Chen, T., Zhang, R., Arjovsky, M.: Improving diffusion models with self-conditioning. *Proceedings of the International Conference on Machine Learning (ICML)* (2023)
11. Cheng, X., Chen, Z.: Multiple video frame interpolation via enhanced deformable separable convolution. *IEEE Transactions on Pattern Analysis and Machine Intelligence* **44**(10), 7029–7045 (2021)
12. Dhariwal, P., Nichol, A.: Diffusion models beat gans on image synthesis. In: *Advances in Neural Information Processing Systems (NeurIPS)* (2021)
13. Feng, Y., Gao, S., Bao, Y., Wang, X., Han, S., Zhang, J., Zhang, B., Yao, A.: Wave: Warping ddim inversion features for zero-shot text-to-video editing. In: *European Conference on Computer Vision*. pp. 38–55. Springer (2024)
14. Gunawan, A., Teodoro, S., Chen, Y., Kim, S.Y., Oh, J., Kim, M.: Omnitext: A training-free generalist for controllable text-image manipulation. arXiv preprint arXiv:2510.24093 (2025)
15. Hertz, A., Mokady, R., Tenenbaum, J.B., Torralba, A., Shamir, A.: Prompt-to-prompt image editing with cross-attention control. arXiv preprint arXiv:2208.01626 (2022)
16. Heusel, M., Ramsauer, H., Unterthiner, T., Nessler, B., Hochreiter, S.: Gans trained by a two time-scale update rule converge to a local nash equilibrium. In: *Neural Information Processing Systems* (2017)
17. Ho, J., Jain, A., Abbeel, P.: Denoising diffusion probabilistic models. In: *Advances in Neural Information Processing Systems (NeurIPS)* (2020)

18. Ho, J., Salimans, T.: Classifier-free diffusion guidance. In: *Advances in Neural Information Processing Systems (NeurIPS)* (2022)
19. Hong, S., Lee, K., Jeon, S.Y., Bae, H., Chun, S.Y.: On exact inversion of dpm-solvers. In: *Proceedings of the IEEE/CVF Conference on Computer Vision and Pattern Recognition*. pp. 7069–7078 (2024)
20. Karras, T., Laine, S., Aittala, M., Hellsten, J., Lehtinen, J., Aila, T.: Analyzing and improving the image quality of stylegan. In: *Computer Vision and Pattern Recognition* (2019)
21. Kim, J., Park, J., Yang, S., Han, D.: Probability density geodesics in image diffusion latent space. *Proceedings of the IEEE/CVF Conference on Computer Vision and Pattern Recognition (CVPR)* (2024)
22. Kim, J., Lee, Z., Cho, D., Jo, S., Jung, Y., Kim, K., Yang, E.: Early timestep zero-shot candidate selection for instruction-guided image editing. In: *Proceedings of the IEEE/CVF International Conference on Computer Vision*. pp. 18844–18854 (2025)
23. Kye, D., Roh, C., Ko, S., Eom, C., Oh, J.: Acevfi: A comprehensive survey of advances in video frame interpolation. *arXiv preprint arXiv:2506.01061* (2025)
24. Labs, B.F., Batifol, S., Blattmann, A., Boesel, F., Consul, S., Diagne, C., Dockhorn, T., English, J., English, Z., Esser, P., Kulal, S., Lacey, K., Levi, Y., Li, C., Lorenz, D., Müller, J., Podell, D., Rombach, R., Saini, H., Sauer, A., Smith, L.: Flux.1 kontext: Flow matching for in-context image generation and editing in latent space (2025), <https://arxiv.org/abs/2506.15742>
25. Lee, S., Kim, H.: Flow-based image morphing. *IEEE Transactions on Image Processing* **21**(2), 820–833 (2012)
26. Li, W., Zhao, J., Zhang, Y., Wang, L.: Layer control: Revisiting layer-wise feature modulation for diffusion models. *arXiv preprint arXiv:2404.12217* (2024)
27. Liang, V.W., Zhang, Y., Kwon, Y., Yeung, S., Zou, J.Y.: Mind the gap: Understanding the modality gap in multi-modal contrastive representation learning. *Advances in Neural Information Processing Systems* **35**, 17612–17625 (2022)
28. Liu, C., Zhang, G., Zhao, R., Wang, L.: Sparse global matching for video frame interpolation with large motion. In: *Proceedings of the IEEE/CVF conference on computer vision and pattern recognition*. pp. 19125–19134 (2024)
29. Liu, H., Xu, C., Yang, Y., Zeng, L., He, S.: Drag your noise: Interactive point-based editing via diffusion semantic propagation. In: *Proceedings of the IEEE/CVF conference on computer vision and pattern recognition*. pp. 6743–6752 (2024)
30. Liu, H., Wang, X., Zhang, L.: Neural image morphing for cross-domain transitions. In: *European Conference on Computer Vision (ECCV)*. pp. 401–418 (2022)
31. Liu, H., Li, C., Li, Y., Li, B., Zhang, Y., Shen, S., Lee, Y.J.: Llava-next: Improved reasoning, ocr, and world knowledge (January 2024), <https://llava-vl.github.io/blog/2024-01-30-llava-next/>
32. Liu, H., Li, C., Wu, Q., Lee, Y.J.: Visual instruction tuning. *Advances in neural information processing systems* **36**, 34892–34916 (2023)
33. Liu, X., Li, Y., He, Q., Zhu, J., Ji, W., Yao, A., Zhu, J.: Interp3d: Correspondence-aware interpolation for generative textured 3d morphing. *ICLR* (2026)
34. Niklaus, S., Liu, F.: Softmax splatting for video frame interpolation. In: *Proceedings of the IEEE/CVF conference on computer vision and pattern recognition*. pp. 5437–5446 (2020)
35. Pardo, A., Pizzati, F., Zhang, T., Pondaven, A., Torr, P., Perez, J.C., Ghanem, B.: Matchdiffusion: Training-free generation of match-cuts. In: *Proceedings of the IEEE/CVF International Conference on Computer Vision*. pp. 14973–14982 (2025)

36. Patashnik, O., Wu, Z., Shechtman, E., Cohen-Or, D., Lischinski, D.: Styleclip: Text-driven manipulation of stylegan imagery. In: Proceedings of the IEEE/CVF international conference on computer vision. pp. 2085–2094 (2021)
37. Peebles, W., Xie, S.: Scalable diffusion models with transformers. In: Proceedings of the IEEE/CVF international conference on computer vision. pp. 4195–4205 (2023)
38. Podell, D., English, Z., Lacey, K., Blattmann, A., Dockhorn, T., Müller, J., Penna, J., Rombach, R.: Sdxl: Improving latent diffusion models for high-resolution image synthesis. arXiv preprint arXiv:2307.01952 (2023)
39. Pont-Tuset, J., Perazzi, F., Caelles, S., Arbeláez, P., Sorkine-Hornung, A., Van Gool, L.: The 2017 davis challenge on video object segmentation. arXiv preprint arXiv:1704.00675 (2017)
40. Poole, B., Jain, A., Barron, J.T., Mildenhall, B.: Dreamfusion: Text-to-3d using 2d diffusion. In: Advances in Neural Information Processing Systems (NeurIPS) (2023)
41. Radford, A., Kim, J.W., Hallacy, C., Ramesh, A., Goh, G., Agarwal, S., Sastry, G., Askell, A., Mishkin, P., Clark, J., Krueger, G., Sutskever, I.: Learning transferable visual models from natural language supervision. Proceedings of the International Conference on Machine Learning (ICML) (2021)
42. Rajković, A., Younes, L.: Riemannian morphing on manifolds. In: International Conference on Computer Vision (ICCV). pp. 1–11 (2023)
43. Rombach, R., Blattmann, A., Lorenz, D., Esser, P., Ommer, B.: High-resolution image synthesis with latent diffusion models. In: Proceedings of the IEEE/CVF conference on computer vision and pattern recognition. pp. 10684–10695 (2022)
44. Ronneberger, O., Fischer, P., Brox, T.: U-net: Convolutional networks for biomedical image segmentation. In: International Conference on Medical image computing and computer-assisted intervention. pp. 234–241. Springer (2015)
45. Russakovsky, O., Deng, J., Su, H., Krause, J., Satheesh, S., Ma, S., Huang, Z., Karpathy, A., Khosla, A., Bernstein, M., Berg, A.C., Fei-Fei, L.: ImageNet Large Scale Visual Recognition Challenge. International Journal of Computer Vision (IJCV) **115**(3), 211–252 (2015). <https://doi.org/10.1007/s11263-015-0816-y>
46. Seo, W., Oh, J., Kim, M.: Bim-vfi: Bidirectional motion field-guided frame interpolation for video with non-uniform motions. In: Proceedings of the Computer Vision and Pattern Recognition Conference. pp. 7244–7253 (2025)
47. Shoemake, K.: Animating rotation with quaternion curves. In: Proceedings of the 12th annual conference on Computer graphics and interactive techniques. pp. 245–254 (1985)
48. Song, J., Meng, C., Ermon, S.: Denoising diffusion implicit models. arXiv preprint arXiv:2010.02502 (2020)
49. Song, Y., Sohl-Dickstein, J., Kingma, D.P., Kumar, A., Ermon, S., Poole, B.: Score-based generative modeling through stochastic differential equations. Proceedings of the International Conference on Learning Representations (ICLR) (2021)
50. Song, Y., Liu, X., Shou, M.Z.: Diffsim: Taming diffusion models for evaluating visual similarity. In: Proceedings of the IEEE/CVF International Conference on Computer Vision. pp. 16904–16915 (2025)
51. Sun, X., Cai, Z., Tang, H., Tai, Y., Yang, J., Zhang, Z.: Morphany3d: Unleashing the power of structured latent in 3d morphing. CVPR (2026)
52. Tang, S., Wu, W., Zhang, Y., Jiang, Y., Li, X., Lin, C., Wang, J., Huang, S., Zhou, K., Lin, D., Luo, P.: T2i-adapter: Learning adapters to dig out more controllable ability for text-to-image diffusion models. In: Proceedings of the IEEE/CVF Conference on Computer Vision and Pattern Recognition (CVPR) (2023)

53. Wang, T., Golland, P., Tenenbaum, J.: Diffusion-based image interpolation via denoising trajectory alignment. In: *Advances in Neural Information Processing Systems (NeurIPS)* (2024)
54. Wang, X., Zhou, B., Curless, B., Kemelmacher-Shlizerman, I., Holynski, A., Seitz, S.M.: Generative inbetweening: Adapting image-to-video models for keyframe interpolation. *arXiv preprint arXiv:2408.15239* (2024)
55. Wang, Y., Wang, W., Yang, Y.: Interpolating between images with diffusion models. *Proceedings of the IEEE/CVF Conference on Computer Vision and Pattern Recognition (CVPR)* (2023)
56. Wolberg, G.: Image morphing: A survey. *The Visual Computer* **14**(8-9), 360–372 (1998)
57. Wu, G., Tao, X., Li, C., Wang, W., Liu, X., Zheng, Q.: Perception-oriented video frame interpolation via asymmetric blending. In: *Proceedings of the IEEE/CVF Conference on Computer Vision and Pattern Recognition*. pp. 2753–2762 (2024)
58. Xue, T., Chen, B., Wu, J., Wei, D., Freeman, W.T.: Video enhancement with task-oriented flow. *International Journal of Computer Vision* (2019)
59. Yang, Z., Yu, Z., Xu, Z., Singh, J., Zhang, J., Campbell, D., Tu, P., Hartley, R.: Impus: Image morphing with perceptually-uniform sampling using diffusion models. *arXiv preprint arXiv:2311.06792* (2023)
60. Yu, S., Kwak, S., Jang, H., Jeong, J., Huang, J., Shin, J., Xie, S.: Representation alignment for generation: Training diffusion transformers is easier than you think. In: *The Thirteenth International Conference on Learning Representations* (2025), <https://openreview.net/forum?id=DJSZGGZYVi>
61. Zeng, W., Shu, Y., Li, Z., Yang, D., Zhou, Y.: Textctrl: Diffusion-based scene text editing with prior guidance control. *Advances in Neural Information Processing Systems* **37**, 138569–138594 (2024)
62. Zhang, K., Zhou, Y., Xu, X., Dai, B., Pan, X.: Diffmorpher: Unleashing the capability of diffusion models for image morphing. In: *Proceedings of the IEEE/CVF Conference on Computer Vision and Pattern Recognition*. pp. 7912–7921 (2024)
63. Zhang, L., Rao, M., Agrawala, M.: Adding conditional control to text-to-image diffusion models. In: *Proceedings of the IEEE/CVF Winter Conference on Applications of Computer Vision (WACV)* (2023)
64. Zhang, R., Isola, P., Efros, A.A., Shechtman, E., Wang, O.: The unreasonable effectiveness of deep features as a perceptual metric. In: *2018 IEEE/CVF Conference on Computer Vision and Pattern Recognition* (2018). <https://doi.org/10.1109/CVPR.2018.00068>
65. Zhang, Z., Chen, H., Zhao, H., Lu, G., Fu, Y., Xu, H., Wu, Z.: Eden: Enhanced diffusion for high-quality large-motion video frame interpolation. In: *Proceedings of the Computer Vision and Pattern Recognition Conference*. pp. 2105–2115 (2025)
66. Zhangli, Q., Jiang, J., Liu, D., Yu, L., Dai, X., Ramchandani, A., Pang, G., Metaxas, D.N., Krishnan, P.: Layout-agnostic scene text image synthesis with diffusion models. In: *2024 IEEE/CVF Conference on Computer Vision and Pattern Recognition (CVPR)*. pp. 7496–7506. IEEE Computer Society (2024)
67. Zope, B., Zope, S.B.: A survey of morphing techniques. *International Journal of Advanced Engineering, Management and Science* **3**(2), 239773 (2017)